Differential adhesion regulates neurite placement via a retrograde zippering mechanism

Authors: Titas Sengupta[1], Noelle L. Koonce[1], Mark W. Moyle[1], Leighton H. Duncan[1], Nabor Vázquez-Martínez[1], Sarah E. Emerson[1], Xiaofei Han[2], Lin Shao[1], Yicong Wu[2], Anthony Santella[3], Li Fan[3], Zhirong Bao[3], William A. Mohler[5], Hari Shroff[2, 4], Daniel A. Colón-Ramos[1, 4, 6,*]

Affiliations:

1. Department of Neuroscience and Department of Cell Biology, Yale University School of Medicine, New Haven, CT 06536, USA.

2. Laboratory of High Resolution Optical Imaging, National Institute of Biomedical Imaging and Bioengineering, National Institutes of Health, Bethesda, MD 20892, USA.

3. Developmental Biology Program, Sloan Kettering Institute, New York, NY 10065, USA.

4. MBL Fellows, Marine Biological Laboratory, Woods Hole, MA 02543, USA

5. Department of Genetics and Genome Sciences and Center for Cell Analysis and Modeling, University of Connecticut Health Center, Farmington, CT 06030, USA.

6. Instituto de Neurobiología, Recinto de Ciencias Médicas, Universidad de Puerto Rico, San Juan 00901, Puerto Rico.

*Correspondence to:

Daniel A. Colón-Ramos, Ph.D.
Department of Neuroscience
Department of Cell Biology
Yale University School of Medicine
333 Cedar Street
SHM B 163D
New Haven, CT 06510
Email: daniel.colon-ramos@yale.edu

Abstract

During development, neurites and synapses segregate into specific neighborhoods or layers within nerve bundles. The developmental programs guiding placement of neurites in specific layers, and hence their incorporation into specific circuits, are not well understood. We implement novel imaging methods and quantitative models to document the embryonic development of the *C. elegans* brain neuropil, and discover that differential adhesion mechanisms control precise placement of single neurites onto specific layers. Differential adhesion is orchestrated via developmentally-regulated expression of the IgCAM SYG-1, and its partner ligand SYG-2. Changes in SYG-1 expression across neuropil layers result in changes in adhesive forces, which sort SYG-2-expressing neurons. Sorting to layers occurs, not via outgrowth from the neurite tip, but via an alternate mechanism of retrograde zippering, involving interactions between neurite shafts. Our study indicates that biophysical principles from differential adhesion govern neurite placement and synaptic specificity *in vivo* in developing neuropil bundles.

Introduction

In brains, neuronal processes or neurites are segregated away from cell bodies into synapse-rich regions termed neuropils: dense structures of nerve cell extensions which commingle to form functional circuits (Maynard, 1962). In both vertebrates and invertebrates, placement of neurites into specific neighborhoods results in a laminar organization of the neuropil (Kolodkin and Hiesinger, 2017, Millard and Pecot, 2018, Nevin et al., 2008, Sanes and Zipursky, 2010, Schürmann, 2016, Soiza-Reilly and Commons, 2014, Xu et al., 2020, Zheng et al., 2018). The laminar organization segregates specific information streams within co-located circuits and is a major determinant of synaptic specificity and circuit connectivity (Baier, 2013, Gabriel et al., 2012, Missaire and Hindges, 2015, Moyle et al., 2021, Nguyen-Ba-Charvet and Chedotal, 2014, White et al., 1986, Xie et al., 2017). The developmental programs guiding placement of neurites along specific layers, and therefore circuit architecture within neuropils, are not well understood.

The precise placement of neurites within layered structures cannot be exclusively explained by canonical tip-directed outgrowth dynamics seen during developmental axon guidance (Tessier-Lavigne and Goodman, 1996). Instead, ordered placement of neurites resulting in layered patterns appears to occur via local cell-cell recognition events. These local cell-cell recognition events are modulated by the regulated expression of specific cell adhesion molecules (CAMs) that place neurites, and synapses, onto layers (Aurelio et al., 2003, Kim and Emmons, 2017, Lin et al., 1994, Petrovic and Hummel, 2008, Poskanzer et al., 2003, Schwabe et al., 2019). For example, studies in both the mouse and fly visual systems have revealed important

82 roles for the regulated spatio-temporal expression of IgSF proteins, such as Sidekick,
83 Dscam and Contactin, in targeting synaptic partner neurons to distinct layers or
84 sublayers (Duan et al., 2014, Sanes and Zipursky, 2010, Tan et al., 2015, Yamagata
85 and Sanes, 2008, Yamagata and Sanes, 2012). In *C. elegans* nerve bundles, neurite
86 position is established and maintained via combinatorial, cell-specific expression of
87 CAMs which mediate local neurite interactions and, when altered, lead to reproducible
88 defects in neurite order within bundles (Kim and Emmons, 2017, Yip and Heiman,
89 2018). How these local, CAM-mediated interactions are regulated during development
90 and how they result in the segregation of neurites into distinct layers, are not well
91 understood.

92 Differential expression of cell adhesion molecules (CAMs) in cells from early
93 embryos can drive their compartmentalization (Foty and Steinberg, 2005, Foty and
94 Steinberg, 2013, Steinberg, 1962, Steinberg, 1963, Steinberg, 1970, Steinberg and
95 Takeichi, 1994). This compartmentalization is in part regulated by biophysical principles
96 of cell adhesion and surface tension which can give rise to tissue-level patterns and
97 boundaries (Canty et al., 2017, Duguay et al., 2003, Erzberger et al., 2020, Foty et al.,
98 1996, Schotz et al., 2008). For example, morphogenic developmental processes such
99 as the patterning of the *Drosophila* germline and retina, the germ layer organization in
100 zebrafish, and the sorting of motor neuron cell bodies into discrete nuclei in the ventral
101 spinal cord can be largely explained via differential adhesion mechanisms and cortical
102 contraction forces that contribute to cell sorting (Bao and Cagan, 2005, Bao et al., 2010,
103 Godt and Tepass, 1998, Gonzalez-Reyes and St Johnston, 1998, Krieg et al., 2008,
104 Price et al., 2002, Schotz et al., 2008). While differential adhesion is best understood in

105 the context of the sorting of cell bodies in early embryogenesis, recent
106 neurodevelopmental work supports that this mechanism influences sorting of neuronal
107 processes *in vivo* as well. For example, differential expression of N-cadherin in the
108 *Drosophila* visual system underlies the organization of synaptic-partnered neurites
109 (Schwabe et al., 2019), where changes in the relative levels of N-cadherin are sufficient
110 to determine placement of neurites within nerve bundles. Whether differential adhesion
111 acts as an organizational principle within layered neuropils to regulate precise
112 placement of neurites is not known.

113 Here we examine the developmental events that lead to placement of the AIB
114 interneurons in the *C. elegans* nerve ring. The *C. elegans* nerve ring is a layered
115 neuropil, with specific strata functionally segregating sensory information and motor
116 outputs (Brittin et al., 2021, Moyle et al., 2021, White et al., 1986). A highly
117 interconnected group of neurons referred to as the 'rich club' neurons, and which
118 include interneuron AIB, functionally link distinct strata via precise placement of their
119 neurites (Moyle et al., 2021, Sabrin et al., 2019, Towlson et al., 2013). Each AIB
120 interneuron projects a single neurite, but segments of that single neurite are placed
121 along distinct and specific layers in the *C. elegans* nerve ring (Fig. 1). The sequence of
122 events resulting in the precise placement of AIB along defined nerve ring layers is
123 unexplored, primarily owing to limitations in visualizing these events *in vivo* during
124 embryonic stages.

125 We implemented novel imaging methods and deep learning approaches to yield
126 high-resolution images of AIB during embryonic development. We discovered that
127 placement of the AIB neurite depends on coordinated retrograde zippering mechanisms

that align segments of the AIB neurite onto specific neuropil layers. Quantitative analysis and modeling of our *in vivo* imaging data revealed that biophysical principles of differential adhesion influence the observed retrograde zippering mechanisms that result in the sorting of the AIB neurite shaft onto distinct neuropil strata. We performed genetic screens to identify the molecular mechanisms underpinning these differential adhesion mechanisms, discovering a role for the IgCAM receptor *syg-1* and its ligand, *syg-2*. We determined that *syg-2* acts in AIB to instruct neurite placement across strata, while *syg-1* is required non-cell autonomously, and at specific layers. Temporally-regulated expression of SYG-1 alters adhesive forces during development to sort segments of AIB onto specific layers. Ectopic expression of SYG-1 predictably affects differential adhesion across layers, repositioning the AIB neurite segments in a SYG-2-dependent manner. Our findings indicate that conserved principles of differential adhesion drive placement of neurites, and *en passant* synaptic specificity, in layered neuropils.

Results

Examination of AIB neurite architecture in the context of the nerve ring strata

First, we characterized the precise placement and synaptic distribution of the AIB neurite within the nerve ring neuropil strata. From electron microscopy connectome datasets and *in-vivo* imaging, we observed that the AIB neurite is unipolar, with its

150 single neurite placed along two distinct and specific strata of the nerve ring (Fig. 1,
151 Supplementary Movies 1-3).

152 Connectomic studies have identified AIB as a “rich club” neuron, a connector hub
153 that links nodes in different functional modules of the brain (Sabrin et al., 2019, Towlson
154 et al., 2013). We observed that AIB’s role as a connector hub was reflected in its
155 architecture within the context of the layered nerve ring (Fig. 1K-N, Supplementary Fig.
156 1, Supplementary Fig. 2). For example, the AIB neurite segment in the posterior
157 neighborhood is enriched in postsynaptic specializations, enabling it to receive sensory
158 information from the adjacent sensory neurons that reside in that neighborhood
159 (Supplementary Fig. 2; (White et al., 1983, White et al., 1986)). AIB relays this sensory
160 information onto the anterior neighborhood, where the AIB neurite elaborates
161 presynaptic specializations that innervate neighboring motor interneurons (Fig. 1D, E, I,
162 J; Supplementary Fig. 2A-G, Supplementary Movie 5). The architecture of AIB is
163 reminiscent of that of amacrine cells of the inner plexiform layer (Demb and Singer,
164 2012, Kolb, 1995, Kunzevitzky et al., 2013, Robles et al., 2013, Strettoi et al., 1992,
165 Taylor and Smith, 2012), which serve as hubs by distributing their neurites and
166 synapses across distinct and specific sublaminae of the vertebrate retina (Marc et al.,
167 2014). We set out to examine how this architecture was laid out during development.

168

169 A retrograde zippering mechanism positions the AIB neurites in the 170 anterior neighborhood during embryonic development

171 Prior to this study, using characterized cell-specific promoters, AIB could be
172 visualized in larvae (Altun et al., 2008, Kuramochi and Doi, 2019) but not in embryos,

173 when placement of AIB into the neighborhoods is specified (Supplementary Fig. 2A
174 shows that by earliest postembryonic stage, L1, AIB neurite placement is complete,
175 indicating placement occurs in the embryo). Moreover, continuous imaging of
176 neurodevelopmental events in embryos, necessary for documenting AIB development,
177 presents unique challenges regarding phototoxicity, speeds of image acquisition as it
178 relates to embryonic movement, and the spatial resolution necessary to discern multiple
179 closely-spaced neurites in the embryonic nerve ring (Wu et al., 2011). These barriers
180 prevented documentation of AIB neurodevelopmental dynamics. To address these
181 challenges, we first adapted a subtractive labeling strategy for sparse labeling and
182 tracking of the AIB neurites in embryos (detailed in Methods, Supplementary Fig. 3A-C,
183 Supplementary Movie 6, (Armenti et al., 2014)). We then adapted use of novel imaging
184 methods, including dual-view light-sheet microscopy (diSPIM) (Kumar et al., 2014, Wu
185 et al., 2013) for long-term isotropic imaging, and a triple-view line-scanning confocal
186 imaging and deep-learning framework for enhanced resolution (Supplementary Fig.
187 3D,E; (Weigert et al., 2018, Wu et al., 2016); Wu et al., in prep).

188 Using these methods, we observed that the AIB neurites enter the nerve ring
189 during the early embryonic elongation phase, ~400 minutes post fertilization (m.p.f). The
190 two AIB neurites then circumnavigate the nerve ring at opposite sides of the neuropil -
191 both AIBL and AIBR project dorsally along the posterior neighborhood, on the left and
192 right-hand sides of the worm, respectively (Fig. 2A,B). Simultaneous outgrowth of AIBL
193 and AIBR neurons in the posterior neighborhood results in their neurites
194 circumnavigating the ring and meeting at the dorsal midline of the nerve ring (Fig. 2C).

195 Therefore, proper placement of the proximal segment of the AIB neurite in the posterior
196 neighborhood occurs by AIB outgrowth along neurons in this neighborhood (Fig. 2A-F).
197 After meeting at the dorsal midline, instead of making a shift to the anterior
198 neighborhood (as expected from the adult AIB neurite morphology – see Fig. 1M,N), the
199 AIB neurites, surprisingly, continue growing along the posterior neighborhood (Fig.
200 2C,D; 480 m.p.f.). At approximately 505 m.p.f., each AIB neurite separates from the
201 posterior neighborhood, starting at its growth cone, by growing tangentially to the
202 posterior neighborhood (the posterior neighborhood is marked in Fig. 2A-G by its lateral
203 counterpart, i.e., the other AIB, also see Supplementary Fig. 3I,J). The departure of the
204 AIB growth cone occurs due to the AIB neurite growing in a straight path trajectory
205 instead of following the bending nerve ring arc (Supplementary Fig. 3I,J). Because it
206 has been documented that axons tend to 'grow straight' on surfaces lacking adhesive
207 forces that instruct turning (Katz, 1985), we hypothesize that the observed exit (via
208 'straight outgrowth') could result from decreased adhesion to the posterior
209 neighborhood (Supplementary Fig. 3I,J).
210 As it grows tangentially to the posterior neighborhood, the AIB neurite cuts
211 orthogonally through the nerve ring and towards the anterior neighborhood
212 (Supplementary Fig. 3I,J). Upon intersecting the anterior neighborhood, the AIB neurite
213 reengages with the arc of the nerve ring. At this developmental stage (Fig 2I), only 3.9%
214 of the AIB distal neurite is placed in the anterior neighborhood, with the remainder still
215 being positioned in the posterior neighborhood and between neighborhoods. Following
216 this, we observed a repositioning of the AIB neurite, but not via expected tip-directed
217 fasciculation. Instead, the entire shaft of the distal AIB neurite was peeled away from

218 the posterior neighborhood and repositioned onto the anterior neighborhood, starting
219 from the tip of the neurite and progressively 'zippering' in a retrograde fashion towards
220 the cell body (Fig. 2J,K; the overlap of the AIB neurite with the anterior neighborhood
221 increased from 3.9% at 515 m.p.f. to 30.4% at 530 m.p.f. and 71.7% at 545 m.p.f.).
222 Retrograde zippering stopped at the dorsal midline of the nerve ring (~545 m.p.f.),
223 resulting in the AIB architecture observed in postembryonic larval and adult stages (Fig.
224 2L). The progressive zippering of the AIB neurite onto the anterior neighborhood occurs
225 concurrently with its separation from the posterior neighborhood (Fig. 2M), a converse
226 process which we refer to as 'unzippering'. The *in vivo* developmental dynamics of AIB
227 repositioning, via retrograde zippering onto the anterior neighborhood, are reminiscent
228 of dynamics observed in cultures of vertebrate neurons in which biophysical forces drive
229 'zippering' of neurite shafts, and the bundling of neurons (Smit et al., 2017).
230

231 **Biophysical modeling of AIB developmental dynamics is consistent with**
232 **differential adhesion leading to retrograde zippering**

233 Dynamics of neurite shaft zippering have been previously documented (Barry et
234 al., 2010, Voyiadjis et al., 2011) and modeled in tissue culture cells (Smit et al., 2017),
235 and described as resulting from two main forces: neurite-neurite adhesion (represented
236 as "S") and mechanical tension (represented as "T"). To better understand the
237 underlying mechanisms of AIB neurite placement, we analyzed AIB developmental
238 dynamics in the context of these known forces that affect neurite zippering. In each
239 neighborhood, the developing AIB neurite experiences two forces: (i) adhesion to
240 neurons in that neighborhood and (ii) tension due to mechanical stretch. As the neurite

241 zippers and unzippers, it has a velocity in the anterior neighborhood (a zippering
242 velocity, v_{zip}) and a velocity in the posterior neighborhood (an unzippering velocity,
243 v_{unzip}) (Fig. 3 and Supplementary Note). These velocities are related to the forces on
244 the neurite by the following equation:
245

246 $$v_{zip} + v_{unzip} = \frac{(S_{anterior} - S_{posterior})}{\eta} - \frac{\Delta T}{\eta}(1 - cos\theta)$$

247

248 where v_{zip} = zippering velocity, v_{unzip} = unzippering velocity, $S_{anterior} - S_{posterior}$ =
249 difference between adhesive forces in the two neighborhoods, $\Delta T = T_{anterior} -$
250 $T_{posterior}$ = difference between tension acting on the AIB neurite in the two
251 neighborhoods, η = friction constant (see Supplementary Note) and θ = angle of the AIB
252 neurite to the neighborhoods (Fig. 3 and Supplementary Note). Since the above
253 biophysical equation defines the relationship between velocities and forces, we
254 measured the velocities of the neurite from our time-lapse images to make predictions
255 about the forces on the neurite.

256 Time lapse images and measurements of the developmental dynamics showed
257 that zippering and unzippering takes place concurrently: zippering on to the anterior
258 neighborhood and unzippering from the posterior one (Fig. 3C). Between 505-545
259 m.p.f., the average length of the AIB neurite that is placed in the anterior neighborhood
260 (4.49 μm) by retrograde zippering is similar to the length that is unzippered from the
261 posterior neighborhood (4.13 μm). Assuming, based on previous studies (Smit et al.,
262 2017), that the tension forces are uniformly distributed along the neurite (and therefore

263 $\Delta T = T_{anterior} - T_{posterior} = 0$), zippering and unzippering velocities arise from a
264 difference in adhesion ($S_{anterior} - S_{posterior} > 0$) (see Supplementary Note).

265 Measurements of *in vivo* zippering velocities (Fig. 3D) support this hypothesis.
266 Examination of our time-lapse images revealed that AIB neurite zippering onto the distal
267 neighborhood takes place at higher velocities at later timepoints (with mean zippering
268 velocity increasing from 0.09 μm/min at 515 mins to 0.34 μm/min at 530 mins) (Fig. 3D).
269 This increased velocity, or acceleration, is a hallmark of force imbalance and consistent
270 with a net increase in adhesive forces in the anterior neighborhood during the period in
271 which zippering takes place. We note that retrograde zippering comes to a stop
272 precisely at the dorsal midline, likely owing to the adhesion and tension forces on the
273 neurite in the two neighborhoods balancing out at this point. Together, the
274 developmental dynamics observed for AIB neurite placement are consistent with
275 relative changes in adhesive forces between the neighborhoods. This suggests that
276 dynamic mechanisms resulting in differential adhesion might govern AIB neurite
277 repositioning.

278

279 **SYG-1 and SYG-2 regulate precise placement of the AIB neurite to the**
280 **anterior neighborhood**

281 To identify the molecular mechanism underpinning differential adhesion for AIB
282 neurodevelopment, we performed forward and reverse genetic screens. We discovered
283 that loss-of-function mutant alleles of *syg-1* and *syg-2*, which encode a pair of
284 interacting Ig family cell adhesion molecules (IgCAMs), display significant defects in the
285 placement of the AIB neurite. In wild type animals, we reproducibly observed complete

286 overlap between the AIB distal neurite and neurons in the anterior neighborhood (Fig.
287 4A-D), consistent with EM characterizations (Supplementary Fig. 2A,B). In contrast,
288 76.3% of *syg-1(ky652)* animals and 60% of *syg-2(ky671)* animals (compared to 1.8% of
289 wild type animals) showed regions of AIB detachment from neurons specifically in the
290 anterior neighborhood (Fig. 4E-L; we note we did not detect defects in general
291 morphology of the nerve ring, in the length of the AIB distal neurite, or in position of the
292 AIB neurite in the posterior neighborhood for these mutants, Supplementary Fig. 4). In
293 the *syg-1(ky652)* and *syg-2(ky671)* animals that exhibit defects in AIB neurite
294 placement, we found that 21.49±4.0% and 17.33±3.9% (respectively) of the neurite
295 segment in the anterior neighborhood is detached from the neighborhood (Fig. 4M). Our
296 findings indicate that SYG-1 and SYG-2 are required for correct placement of AIB,
297 specifically to the anterior neighborhood.

298 The IgCAMs SYG-1 and SYG-2 are a receptor-ligand pair that has been best
299 characterized in the context of regulation of synaptogenesis in the *C. elegans* egg-
300 laying circuit (Shen and Bargmann, 2003, Shen et al., 2004). SYG-1 (Rst and Kirre in
301 *Drosophila* and Kirrel1/2/3 in mammals) and SYG-2 (Sns and Hibris in Drosophila, and
302 Nephrin in mammals) orthologs also act as multipurpose adhesion molecules in varying
303 conserved developmental contexts (Bao and Cagan, 2005, Bao et al., 2010, Chao and
304 Shen, 2008, Garg et al., 2007, Neumann-Haefelin et al., 2010, Ozkan et al., 2014,
305 Oztokatli et al., 2012, Serizawa et al., 2006, Shen and Bargmann, 2003, Shen et al.,
306 2004, Strunkelnberg et al., 2001). In most of the characterized *in vivo* contexts, SYG-1
307 has been shown to act heterophilically with SYG-2 (Dworak et al., 2001, Ozkan et al.,
308 2014, Shen et al., 2004). Consistent with SYG-1 and SYG-2 acting jointly for precise

309 placement of the AIB neurite *in vivo*, we observed that a double mutant of the *syg-*
310 *1(ky652)* and *syg-2 (ky671)* loss-of-function alleles did not enhance the AIB distal
311 neurite placement defects as compared to either single mutant (Fig. 4N).

312 To determine the site of action of these two molecules, we expressed them cell-
313 specifically in varying tissues. We observed that SYG-2 expression in AIB was sufficient
314 to rescue the AIB distal neurite placement defects in the *syg-2(ky671)* mutants,
315 suggesting that SYG-2 acts cell autonomously in AIB. While expression of wild-type
316 SYG-1 (via a cosmid) rescued AIB neurite placement onto the anterior neighborhood,
317 expression of SYG-1 using an AIB cell-specific promoter did not (Fig. 4N), consistent
318 with SYG-1 regulating AIB neurite placement cell non-autonomously.

319

320 **Increased local expression of SYG-1 in the anterior neighborhood**
321 **coincides with zippering of the AIB neurite onto this neighborhood**

322 To understand how SYG-1 coordinates placement of the AIB neurite, we examined
323 the expression of transcriptional and translational reporters of SYG-1 in the nerve ring of
324 wild type animals. In postembryonic, larva-stage animals (L3 and L4), we observed
325 robust expression of the *syg-1* transcriptional reporter in a banded pattern in ~20
326 neurons present in the AIB posterior and anterior neighborhoods, with specific
327 enrichment in the anterior neighborhood (Fig. 5A-E). The SYG-1 translational reporter,
328 which allowed us to look at SYG-1 protein accumulation, also showed a similar
329 expression pattern (Fig. 5F-I). To understand how SYG-1 regulates placement of the
330 AIB neurite during development, we examined spatiotemporal dynamics of expression

331 of SYG-1 during embryogenesis at the time of AIB neurite placement (400-550 m.p.f.)
332 (Fig. 2), using both the transcriptional and translational *syg-1* reporters.

333 Prior to 470 m.p.f., *syg-1* reporter expression in the nerve ring was primarily
334 restricted to a single band corresponding to the AIB posterior neighborhood (Fig.
335 5K,O,O'). This coincides with periods of outgrowth and placement of the AIB neurons in
336 the posterior neighborhood. However, over the subsequent three hours of
337 embryogenesis (470-650 m.p.f.), SYG-1 expression levels progressively increase in the
338 anterior neighborhood while decreasing in the posterior neighborhood (Fig. 5L-R',
339 Supplementary Fig. 5, Supplementary Movie 7). The change in expression levels of
340 SYG-1 across neighborhoods coincides with the relocation of the AIB neurite, from the
341 posterior to the anterior neighborhood via retrograde zippering (Fig. 5S). Our
342 observations *in vivo* are consistent with reported SYG-1 expression levels from
343 embryonic transcriptomics data (Packer et al., 2019), which demonstrate similar SYG-1
344 expression changes in neurons in the anterior and posterior neighborhoods of AIB
345 (Supplementary Table 1). The transcriptomic studies also demonstrate a ten-fold
346 increase in SYG-2 transcript levels in AIB at the time in which the AIB neurite transitions
347 between neighborhoods (and consistent with our findings that SYG-2 acts cell
348 autonomously in AIB). Together with the biophysical analyses, our data suggests that
349 spatiotemporal changes in SYG-1 and SYG-2 expression might result in changes in
350 forces that drive differential adhesion of AIB neurites via retrograde zippering of their
351 axon shafts.

352

353 **Ectopic *syg-1* expression is sufficient to alter placement of the AIB distal**
354 **neurite**

355 To test whether coincident SYG-1 expression in the anterior neighborhood was
356 responsible for repositioning of AIB to that neighborhood, we set to identify and
357 manipulate the sources of SYG-1 expression. We found that increases of SYG-1 in the
358 anterior neighborhood were caused by (i) ingrowth of SYG-1-expressing neurons into
359 the anterior neighborhood and (ii) onset of *syg-1* expression in neurons of the anterior
360 neighborhood (Supplementary Fig. 5). We observed strong and robust SYG-1
361 expression in the RIM neurons, the primary postsynaptic partner of AIB, both in
362 embryonic and postembryonic stages, leading us to hypothesize that SYG-1 expression
363 in RIM neurons contributes to AIB neurite placement (Supplementary Fig. 6). To test
364 this hypothesis, we ablated RIM neurons. We observed that RIM ablations result in
365 defects in AIB neurite placement which phenocopied those seen for *syg-1* loss-of-
366 function mutants (Supplementary Fig. 7). We also observed that expression of SYG-1
367 specifically in RIM and RIC neurons in *syg-1(ky652)* mutants was sufficient to position
368 the AIB distal neurite along these neurons (Supplementary Fig. 7P-Q').

369 If differences in SYG-1 expression level between the neighborhoods results in
370 differential adhesion, and consequent relocation of the AIB distal neurite from the
371 posterior to the anterior neighborhood, then purposefully altering these differences
372 should predictably alter the position of the AIB neurite. We aimed to test this hypothesis
373 by inverting the adhesion differential through the overexpression of SYG-1 in the
374 posterior neighborhood (see Methods). Unlike wild type and *syg-1* mutants (Fig. 6A-F,
375 Supplementary Fig. 8A,B), animals with ectopic *syg-1* expression in the posterior

376 neighborhood displayed a gain-of-function phenotype, in which the AIB distal neurite
377 remained partially positioned in the posterior neighborhood throughout postembryonic
378 larval stages (Fig. 6G-J, Supplementary Fig. 8A,B). Importantly, these gain-of-function
379 effects caused by ectopic expression of SYG-1 are not observed in a *syg-2(ky671)*
380 mutant background, consistent with SYG-2 expression in AIB being required for AIB's
381 repositioning to the SYG-1 expressing layers. Our findings indicate that inverting the
382 adhesion differential via enrichment of SYG-1 in the 'wrong' neighborhood predictably
383 affects relocation of the AIB distal neurite in a way that is consistent with differential
384 adhesion mechanisms.

385 We reasoned that if differential adhesion mechanisms were driving zippering of
386 the AIB neurite during development, expression of the SYG-1 ectodomain would be
387 sufficient to drive the ectopic interactions upon misexpression (Chao and Shen, 2008,
388 Galletta et al., 2004, Gerke et al., 2003). Indeed, expression of the SYG-1 ectodomain
389 in the posterior neighborhood resulted in gain-of-function phenotypes for AIB neurite
390 placement, similar to those seen with misexpression of full-length SYG-1 (although
391 penetrance of these effects was lower than that observed with full-length SYG-1).
392 Consistent with the importance of adhesion-based mechanisms in the observed
393 phenotypes, ectopic expression of the SYG-1 endodomain in the posterior
394 neighborhood did not result in mislocalization of AIB (Supplementary Fig. 8A,B).

395

396 **AIB neurite placement by retrograde zippering, and presynaptic assembly**
397 **are coordinated during development**

398 AIB displays a polarized distribution of pre- and postsynaptic specializations, and
399 these specializations specifically localize to the neurite segments occupying the anterior
400 and posterior neighborhoods, respectively. The placement of the AIB neurite in the
401 anterior and posterior neighborhoods and its synaptic polarity underlies its role as a
402 connector hub across layers (Sabrin et al., 2019, Towlson et al., 2013). To understand
403 how the distribution of presynaptic specializations relates to the placement of the AIB
404 neurite, we imaged the subcellular localization of presynaptic protein RAB-3 during AIB
405 embryonic development. We observed that presynaptic proteins populate the AIB
406 neurite starting from the tip towards the dorsal midline, in a retrograde pattern
407 reminiscent of the retrograde zippering that places the AIB neurite in the anterior
408 neighborhood (Fig. 7A-I). The timing of formation of presynaptic sites suggested that
409 that the process of synaptogenesis closely followed the retrograde zippering
410 mechanisms of AIB repositioning, indicating that zippering, and presynaptic assembly,
411 coincide during development. Consistent with the importance of AIB neurite placement
412 in the anterior neighborhood for correct synaptogenesis, we observed that in *syg-*
413 *1(ky652)*, RAB-3 signal was specifically and consistently reduced in regions of the AIB
414 distal neurite incapable of repositioning to the anterior neighborhood (Supplementary
415 Fig. 8C-N). Overall, our study identified a role for differential adhesion in regulating
416 neurite placement via retrograde zippering, which in turn influences synaptic specificity
417 onto target neurons (Fig. 7J).
418

419 **Discussion**

420 The precise assembly of the cellular architecture of AIB in the context of the
421 layered nerve ring neuropil underwrites its role as a “rich-club” neuron. AIB was
422 identified, through graph theory analyses, as a rich-club neuron (Towlson et al., 2013) -
423 a connector hub with high betweeness centrality, which links nodes of the *C. elegans*
424 neural networks with high efficiency. We observe that the AIB neurite segments are
425 precisely placed on distinct functional layers of the nerve ring neuropil, and that the
426 placement of these segments, in the context of the pre- and postsynaptic polarity of the
427 neurite, enables AIB to receive inputs from one neighborhood and relay information to
428 the other, thereby linking otherwise modular and functionally distinct layers. Our
429 connectomic analyses and *in vivo* imaging reveal that these features of AIB architecture
430 are stereotyped across examined *C. elegans* animals, even as early as the first larval
431 stage, L1. They are also evolutionarily conserved in nematodes, as examination of AIB
432 in the connectome of the nematode *Pristionchus pacificus,* which is separated from *C.*
433 *elegans* by 100 million years of evolutionary time, revealed similar design principles
434 (Hong et al., 2019). The architecture of AIB is reminiscent to that seen for other “nexus
435 neurons” in layered neuropils, such as AII amacrine cells in the inner plexiform layer of
436 the vertebrate retina (Marc et al., 2014). Like AIB, All amacrine cells receive inputs from
437 one laminar neighborhood (rod bipolar axon terminals in “lower sublamina b”) and
438 produce outputs onto a different neighborhood (ganglion cell dendrites in “sublamina a”)
439 (Kolb, 1995, Strettoi et al., 1992). For these nexus neurons, as for AIB, the precise
440 placement within neuropil layers is critical for their function and connectivity. We now
441 demonstrate that for AIB, this precise placement is governed via differential adhesion
442 instructed by the layer-specific expression of IgCAM SYG-1. Interestingly, other ‘rich-

443 club' neurons that emerged from connectomic studies, such as AVE and RIB, are also
444 placed along SYG-1-expressing nerve ring layers, suggesting that similar, SYG-1
445 dependent and layer-specific mechanisms could underpin placement of these neurons.

446 Differential adhesion acts via retrograde zippering mechanisms to position AIB
447 across multiple and specific layers. We established new imaging paradigms to
448 document *in vivo* embryonic development of AIB, and observed that the sorting of its
449 distal neurite segment onto the anterior neighborhood occurs, not via tip-directed
450 fasciculation as we had anticipated, but via neurite-shaft retrograde zippering. Zippering
451 mechanisms had been previously documented (Barry et al., 2010, Voyiadjis et al.,
452 2011), and modeled, for tissue culture cells, where they were shown to act via
453 biophysical forces of tension and adhesion (Smit et al., 2017). We now demonstrate that
454 retrograde zippering also acts *in vivo* to precisely place segments of the AIB neurite in
455 specific neuropil layers.

456 Retrograde zippering depends on differential adhesion across layers, and is
457 instructed by the dynamic expression of SYG-1, and its interaction with the SYG-2
458 expressing AIB neurons. The observed role of SYG-1 in the nerve ring is reminiscent of
459 the role of the SYG-1 and SYG-2 mammalian orthologs, Kirrel2 and Kirrel3, in axon
460 sorting in the olfactory system (Serizawa et al., 2006), and consistent with observations
461 in *C. elegans* that *syg-2* loss of function mutants result in defasciculation defects of the
462 HSNL axon (Shen et al., 2004). Our findings are also consistent with studies on the
463 roles of SYG-1 and SYG-2 Drosophila orthologues, Hibris and Roughest, in tissue
464 morphogenesis of the pupal eye (Bao and Cagan, 2005). In these studies, Hibris and
465 Roughest were shown to instruct complex morphogenic patterns by following simple,

466 adhesion and surface energy-based biophysical principles that contributed to
467 preferential adhesion of specific cell types. We now demonstrate that similar biophysical
468 principles of differential adhesion might help organize neurite placement within
469 heterogeneous tissues, such as neuropils in nervous systems.

470 SYG-1 and SYG-2 coordinate developmental processes that result in synaptic
471 specificity for the AIB interneurons. Synapses in *C. elegans* are formed *en passant*, or
472 along the length of the axon, similar to how they are assembled in the CNS for many
473 circuits (Jontes et al., 2000, Koestinger et al., 2017). Placement of neurites within
474 layers therefore restrict synaptic partner choice. We examined how these events of
475 placement, and synaptogenesis, were coordinated for the AIB interneurons and
476 observed coincidence of presynaptic assembly and retrograde zippering of the AIB
477 neurite. SYG-1 and SYG-2 were identified in *C. elegans* for their role in synaptic
478 specificity (Shen and Bargmann, 2003, Shen et al., 2004), and the assembly of synaptic
479 specializations can result in changes in the cytoskeletal structure and adhesion
480 junctions (Missler et al., 2012). We hypothesize that coordinated assembly of synaptic
481 sites during the process of retrograde zippering could provide forces that stabilize
482 zippered stretches of the neurite. These could in turn “button” and fasten the AIB neurite
483 onto the anterior layer, securing its relationship with its postsynaptic partner. Consistent
484 with this hypothesis, we observe that ablation of one of its main postsynaptic partners,
485 the RIM neurons, results in defects in AIB placement in the anterior neighborhood.
486 Given the important role of adhesion molecules in coordinating cell-cell interactions and
487 synaptogenesis (Sanes and Zipursky, 2010, Sanes and Zipursky, 2020, Tan et al.,
488 2015, Yamagata and Sanes, 2008, Yamagata and Sanes, 2012), we speculate that

489 adhesion molecules involved in synaptogenesis and neurite placement within layered
490 neuropils might similarly act to coordinate differential adhesion and synaptogenesis onto
491 target neurons.

492 Zippering mechanisms via affinity-mediated adhesion might help instruct
493 neighborhood coherence while preserving 'fluid', or transient interactions among
494 neurites within neuropil structures. Analysis of connectome data and examination of
495 neuronal adjacencies within the nerve ring neuropil revealed that contact profiles for
496 single neurons vary across animals indicative of fluid or transient interactions during
497 development (Moyle et al., 2021). Yet neuropils have a stereotyped and layered
498 architecture encompassing specific circuits. We hypothesize that dynamic expression of
499 adhesion molecules help preserve tissue organization in tangled neuropils via the
500 creation of affinity relationships of relative strengths. These relationships, in the context
501 of outgrowth decisions of single neurites, would contribute to the sorting of neurites onto
502 specific strata. We propose that sorting of neurite into strata would happen through
503 biophysical interactions not unlike those reported for morphogenic events in early
504 embryos and occurring via differential adhesion (Steinberg, 1962, Foty and Steinberg,
505 Steinberg and Gilbert, 2004). Spatiotemporally restricted expression of CAMs in layers,
506 as we observe for SYG-1 and has been observed for other CAMs in layered neuropils
507 (Sanes and Zipursky, 2010, Sanes and Zipursky, 2020, Tan et al., 2015, Yamagata and
508 Sanes, 2008, Yamagata and Sanes, 2012) would then result in dynamic affinity-
509 mediated relationships that preserve neighborhood coherence in the context of 'fluid', or
510 transient interactions among neurites within the neuropil structures.
511

512 **Methods**

513 **Materials Availability**

514 Plasmids and worm lines generated in this study are available upon request (see
515 Supplementary Tables 2 and 3 for details).

516 **Data Availability**

517 The original/source data generated or analyzed during this study are available from the
518 corresponding author upon request.

519

520 **Code Availability**

521 From previously determined adjacencies (Brittin et al., 2018, Brittin et al., 2021, Witvliet
522 et al., 2020), cosine similarities were calculated in Excel, using the formula described in
523 Methods. For computing binary connection matrices for centrality analysis (detailed in
524 Methods below). we used the function “betweenness_bin.m” in the Brain Connectivity
525 Toolbox (Rubinov and Sporns) of MATLAB2020.

526

527 **Maintenance of *C. elegans* strains**

528 *C. elegans* strains were raised at 20°C using OP50 *Escherichia coli* seeded on
529 NGM plates. N2 Bristol is the wild-type reference strain used. Plasmids and transgenic
530 strains generated and used in this study (Supplementary Tables 2 and 3) are available
531 upon request.

532

533 **Molecular biology and generation of transgenic lines**

534 We used Gibson Assembly (New England Biolabs) or the Gateway system
535 (Invitrogen) to make plasmids (Supplementary Table 3) used for generating transgenic
536 *C. elegans* strains (Supplementary Table 2). Detailed cloning information or plasmid
537 maps will be provided upon request. Transgenic strains were generated via
538 microinjection with the construct of interest at 2-100 ng/uL by standard techniques
539 (Mello and Fire). Co-injection markers *unc-122p*: GFP or *unc-122p*: RFP were used.

540 We generated the *syg-1* transcriptional reporter (Fig. 5, Supplementary Fig. 5)
541 by fusing membrane-targeted PH:GFP to a 3.5 kb *syg-1* promoter region as described
542 (Schwarz et al., 2009). The translational reporter was generated by fusing a GFP-
543 tagged *syg-1b* cDNA using the same promoter (Fig. 5). For cell-specific SYG-1
544 expression, full length SYG-1, SYG-1 ecto (extracellular +TM domain - amino acids 1-
545 574, (Chao and Shen, 2008)) or SYG-1 endo (signal peptide+TM domain+cytoplasmic
546 domain – amino acids 1-31+526-574) were used.

547 For cell-specific labeling and expression in larvae, we used an *inx-1* promoter for
548 AIB (Altun et al., 2008), a *ceh-36* promoter for AWC and ASE (Kim et al., 2010) and *tdc-*
549 *1*, *gcy-13* and *cex-1* promoters for RIM (Greer et al., 2008, Piggott et al., 2011).

550

551 **SNP mapping and Whole-Genome Sequencing**

552 We performed a visual forward genetic screen in an integrated wild type
553 transgenic strain (*olaIs67*) with AIB labeled with cytoplasmic mCherry and AIB
554 presynaptic sites labeled with GFP:RAB-3. Ethyl methanesulfonate (EMS) mutagenesis
555 was performed and animals were screened for defects in placement of the AIB neurite,

556 or presynaptic distribution. We screened for these same phenotypes in our reverse
557 genetic screens as well, where we crossed the marker strain (*olaIs67*) to characterized
558 mutant alleles. We screened F2 progeny on a Leica DM 5000 B compound microscope
559 with an HCX PL APO 63x/1.40–0.60 oil objective.

560 Mutants from forward genetic screens were out-crossed six times to wild type
561 (N2) animals and mapped via single-nucleotide polymorphism (SNP) (Davis et al.,
562 2005) and whole-genome sequencing as previously described (Sarin et al., 2008). We
563 analyzed the results using the Galaxy platform (https://galaxyproject.org/news/cloud-
564 map/, EMS variant density mapping workflow (Minevich et al., 2012).

565

566 **Confocal imaging of *C. elegans* larvae and image processing**

567 We used an UltraView VoX spinning disc confocal microscope with a 60x CFI
568 Plan Apo VC, NA 1.4, oil objective on a NikonTi-E stand (PerkinElmer) with a
569 Hamamatsu C9100–50 camera. We imaged the following fluorescently tagged fusion
570 proteins, eGFP, GFP, PH:GFP (membrane-tethered), RFP, mTagBFP1, mCherry,
571 mCherry:PH, mScarlet, mScarlet:PH at 405, 488 or 561 nm excitation wavelength. We
572 anesthetized larval stage 4 animals (unless otherwise mentioned) at room temperature
573 in 10mM levamisole (Sigma) and mounted them on glass slides for imaging. For Fig. 5
574 and the RIM neuron ablation images in Supplementary Fig. 7, larval stage 3 animals
575 were imaged.

576 We used the Volocity image acquisition software (Improvision by Perkin Elmer)
577 and processed our images using Fiji (Schindelin et al., 2012). Image processing

578 included maximum intensity projection, 3D projection, rotation, cropping,
579 brightness/contrast, line segment straightening, and pseudo coloring. All quantifications
580 from confocal images were conducted on maximal projections of the raw data.
581 Pseudocoloring of AIBL and AIBR was performed in Fiji. To achieve this, pixels
582 corresponding to the neurite of either AIBL/R were identified and the rest of the pixels in
583 the image were cleared. This was done for both neurons of the pair and the resulting
584 images were merged. For quantifications from confocal images, n= number of neurons
585 quantified, unless otherwise mentioned.

586

587 **Embryo labeling, imaging and image processing**

588 For labeling of neurites in embryos, we used membrane tethered PH:GFP or
589 mScarlet:PH. A subtractive labeling strategy was employed for AIB embryo labeling
590 (Supplementary Fig. 3A-C) (Armenti et al., 2014, Moyle et al., 2021). Briefly, we
591 generated a strain containing unc-42p::ZF1::PH::GFP and lim-4p::SL2::ZIF-1, which
592 degraded GFP in the sublateral neurons, leaving GFP expression only in the AIB and/or
593 ASH neurons. Onset of twitching was used as a reference to time developmental
594 events. Embryonic twitching is stereotyped and starts at 430 minutes post fertilization
595 (m.p.f) for our imaging conditions.

596 Embryonic imaging was performed via dual-view inverted light sheet microscopy
597 (diSPIM) (Kumar et al., 2014, Wu et al., 2013) and a combined triple-view line scanning
598 confocal/DL for denoising (Wu et al., in prep, also described below) described below.
599 Images were processed and quantifications from images were done using CytoSHOW,

600 an open source image analysis software. CytoSHOW can be downloaded from
601 http://www.cytoshow.org/ as described (Duncan et al., 2019).
602
603 **Triple-view line-scanning confocal/DL**
604 We developed a triple-view microscope that can sequentially capture three
605 specimen views, each acquired using line-scanning confocal microscopy (Wu et al., in
606 prep). Multiview registration and deconvolution can be used to fuse the 3 views (Wu et
607 al., 2016), improving spatial resolution. Much of the hardware for this system is similar
608 to the previously published triple-view system (Wu et al., 2016), i.e., we used two 0.8
609 NA water immersion objectives for the top views and a 1.2 NA water immersion lens
610 placed beneath the coverslip for the bottom view. To increase acquisition speed and
611 reduce photobleaching, we applied a deep-learning framework (Weigert et al., 2018) to
612 predict the triple-view result when only using data acquired from the bottom view. The
613 training datasets were established from 50 embryos (anesthetized with 0.3% sodium
614 azide) in the post-twitching stage, in which the ground truth data were the deconvolved
615 triple view confocal images, and the input data were the raw single view confocal
616 images. These approaches resulted in improved resolution (270nm X 250 nm X
617 335nm).
618
619 **Cell lineaging**
620 Cell lineaging was performed using StarryNite/AceTree (Bao et al., 2006, Boyle
621 et al., 2006, Murray et al., 2006). Light sheet microscopy and lineaging approaches
622 were integrated to uncover cell identities in pre-twitching embryos (Duncan et al., 2019).

623 Lineaging information for promoters is available at http://promoters.wormguides.org.
624 Our integrated imaging and lineaging approaches enabled us to identify a promoter
625 region of *inx-19* which is expressed in the RIM neurons prior to RIM neurite outgrowth
626 (~370 m.p.f.) and in additional neurons in later embryonic stages. The *inx-19p* was one
627 of the promoters used for embryonic ablation of the RIM neurons (described in the next
628 section).
629 In addition, our integrated imaging and lineaging approach also enabled us to identify
630 two promoters with expression primarily in neurons located at the AIB posterior
631 neighborhood (*nphp-4*p and *mgl-1b*p). 4/4 neuron classes that were identified to have
632 *nphp4*p expression are in the AIB posterior neighborhood (ADL/R, ASGL/R, ASHL/R,
633 ASJL/R) and 2/3 neuron classes that were identified to have *mgl-1b*p expression are in
634 the AIB posterior neighborhood (AIAL/R, ADFR) (http://promoters.wormguides.org). We
635 used these promoters to drive ectopic expression of a *syg-1* cDNA specifically in the
636 posterior neighborhood.
637

638 **Caspase-mediated ablation of RIM neurons**

639 The RIM neurons were ablated using a split-caspase ablation system (Chelur
640 and Chalfie, 2007). We generated one set of transgenic strains with co-expression of
641 the p12 and p17 subunit of human Caspase-3, both expressed under *inx-19p* (termed
642 ablation strategy 1), and another set of ablation strains with co-expression of the p12
643 subunit expressed under *inx-19p* and p17 under *tdc-1p* (termed ablation strategy 2)
644 (Supplementary Fig. 7). L3 larvae from the RIM-ablated populations were imaged on the

645 spinning-disk confocal microscope (described in the **'Confocal imaging of C. elegans**
646 **larvae and image processing'** section).

647

648 **Rendering of neurites and contacts in the EM datasets**

649 From available EM datasets (Brittin et al., 2018, Cook et al., 2019, White et al.,
650 1986, Witvliet et al., 2020) we rendered the segmentations of neuron boundaries in 2D
651 using TrakEM2 in Fiji. TrakEM2 segmentations were volumetrically rendered by using
652 the 3D viewer plugin in Fiji (downloaded from https://imagej.net/Fiji#Downloads) and
653 saved as object files (.obj), or by using the 3D viewer in CytoSHOW.

654 To generate 3D mappings of inter-neurite membrane contact, the entire
655 collection of 76,046 segmented neuron membrane boundaries from the JSH TEM
656 datasets (Brittin et al., 2018, White et al., 1986) were imported from TrakEM2 format
657 into CytoSHOW as 2D cell-name-labelled and uniquely color-coded regions of interest
658 (ROIs). To test for membrane juxtaposition, we dilated each individual cell-specific ROI
659 by 9 pixels (40.5 nm) and identified for overlap by comparing with neighboring undilated
660 ROIs from the same EM slice. A collection of 289,012 regions of overlap were recorded
661 as new ROIs, each bearing the color code of the dilated ROI and labeled with both cell-
662 names from the pair of the overlapped ROIs. These "contact patch" ROIs were then
663 grouped by cell-pair-name and rendered via a marching cubes algorithm to yield 3D
664 isosurfaces saved in .obj files. Each of the 8852 rendered .obj files represents all
665 patches of close adjacency between a given pair of neurons, color-coded and labeled
666 by cell-pair name. Selected .obj files were co-displayed in a CytoSHOW3D viewer
667 window to produce views presented in Fig. 1, Supplementary Fig. 1 and 2.

668

669 **Schematic representation of larval *C. elegans***

670 The schematic representations of larval *C. elegans* in Fig. 1 and Supplementary Fig. 6
671 were made using the 3D worm model in OpenWorm (http://openworm.org - 3D Model
672 by Christian Grove, WormBase, CalTech).

673

674 **Quantification and statistical analysis**

675

676 **Cosine similarity analysis for comparing AIB contacts across connectomes**

677 We performed cosine similarity analysis (Han et al., 2012) on AIB contacts in
678 available connectome datasets (Brittin et al., 2018, White et al., 1986, Witvliet et al.,
679 2020). For each available adjacency dataset (Brittin et al., 2021, Moyle et al., 2021,
680 Witvliet et al., 2020), we extracted vectors comprising of the weights of AIB contacts
681 with neurons common to all the datasets. We then performed cosine similarity analysis
682 on these vectors using the formula:

683
$$\frac{\sum_{i=1}^{n} A_i B_i}{\sqrt{\sum_{i=1}^{n} A_i^2}\sqrt{\sum_{i=1}^{n} B_i^2}}$$

684 where A and B are the two vectors under consideration with the symbol “i” denoting the
685 i-th entry of each vector. The similarity values were plotted as a heat map for AIBL and
686 AIBR using Prism. For the datasets L1_0hr, L1_5hr, L1_8hr, L2_23hr, L3_27hr, L4_JSH
687 and Adult_N2U, only the neuron-neuron contacts in the EM sections corresponding to
688 the nerve ring were used (as opposed to the whole connectome).

Betweenness centrality analysis

We analyzed betweenness centrality for two of the available connectomes of different developmental stages (L1 and adult) (Witvliet et al., 2020). By treating individual components (mostly neurons) of a connectome as the vertices of a graph, we use the following definition of Betweenness Centrality for a vertex v,

$$BC(v) = \sum_{s,t:s\neq t\neq v} \frac{\lambda_{st}(v)}{\lambda_{st}}$$

Here $\lambda_{st}(v)$ denotes the number of shortest paths between the vertices s and t, that include vertex v, whereas λ_{st} denotes the total number of shortest paths between the vertices s and t. We finally divide $BC(v)$ by $(N-1)(N-2)/2$ to normalize it to lie between 0 and 1. For our implementation we use the Brain Connectivity Toolbox (Rubinov and Sporns) of MATLAB2020, in particular, the function “betweenness_bin.m” in which we input the binary connectivity matrix (threshold = 0) (Fornito et al., 2016) corresponding to the L1 and adult connectomes (Witvliet et al., 2020). We made a Prism box plot (10 to 90 percentile) of betweenness centrality values of all components in each of the two connectomes and highlighted the betweenness centrality values for AIBL and AIBR.

Representation of AIB from confocal images

708 Since we observed that the proximal and distal neurites of AIBL and AIBR
709 completely align and overlap (Supplementary Fig. 1) in confocal image stacks where the
710 worms are oriented on their side, for representation purposes we have used the upper
711 50% of z-slices in confocal image stacks to make maximum intensity projections. This
712 shows the proximal neurite of AIBL in the context of the distal of AIBR (which has the
713 same anterior-posterior position as the distal neurite of AIBL) (Supplementary Fig. 1), or
714 vice versa.

715

716 **Quantification of penetrance of AIB neurite placement defects and gain-of-**
717 **function phenotypes**

718 The penetrance of defects in AIB neurite placement in the anterior neighborhood
719 in mutant (or ablation) strains was determined by visualizing the AIB neurite and scoring
720 animals with normal or defective anterior neighborhood placement under the Leica
721 compound microscope described. Animals in which the entire distal neurite was placed
722 at a uniform distance from the proximal neurite, for both AIBL and AIBR, were scored as
723 having normal AIB distal neurite placement.

724 The penetrance of the gain-of-function effects in ectopic SYG-1 expression
725 strains was determined by scoring the percentage of animals showing ectopic AIB distal
726 neurite placement in the posterior neighborhood. Animals with part (or whole) of the AIB
727 distal neurite overlapping with the posterior neighborhood were considered as having
728 ectopic AIB placement.

729

730 **Quantification of minimum perpendicular distance between neurites**

731 Minimum perpendicular distances between neurites were measured by creating a
732 straight line selection (on Fiji) between the neurites (perpendicular to one of the
733 neurites) in the region where the gap between them is estimated to be the smallest. The
734 measurements were done on maximum intensity projections of raw confocal image
735 stacks where the worms are oriented on their side (z-stacks acquired along left-right
736 axis of the worm, producing a lateral view of the neurons).

737

738 **Quantification of percent detachment between neurites**

739 The percent detachment for defasciculated neurites (AIB and RIM) is calculated
740 by the formula % detachment = detached length (L_d) x 100 /total length (L_t) (also shown
741 in Fig. 4M). L_d is calculated by making a freehand line selection along the detached
742 region of the RIM neurite and measuring its length and L_t is calculated by making a
743 freehand selection along the RIM neurite for the entire length over which it contacts AIB,
744 and measuring the length of the selection. All the measurements were performed on
745 maximum intensity projections of confocal image stacks where the worms are oriented
746 on their side (z-stacks acquired along left right axis of the worm, producing a lateral
747 view of the neurons).

748

749 **Quantification of relative enrichment of *syg-1* reporter expression in the**
750 **anterior neighborhood**

751 Relative (anterior) enrichment of *syg-1* reporter expression in embryos (Fig. 5S)
752 is calculated using the formula, relative enrichment (*syg-1p*) = mean anterior
753 neighborhood intensity (I_a)/mean posterior neighborhood intensity (I_p). These
754 measurements were done in transgenic embryos co-expressing the AIB reporter and
755 the *syg-1* transcriptional reporter. For calculation of I_p, a freehand line selection was
756 made (using CytoSHOW, http://www.cytoshow.org/, (Duncan et al., 2019)) along the
757 posterior band of *syg-1* expression and mean intensity along the selection was
758 calculated. Same was done for calculation of I_a. The ratios of I_a and I_p were plotted as
759 relative (anterior) enrichment values (Fig. 5S). These values were calculated from 3D
760 projections of deconvolved diSPIM images acquired at intensities within dynamic range
761 (not saturated) at timepoints during embryogenesis (485, 515 and 535 minutes post
762 fertilization), when the AIB neurite grows and is placed into the posterior and anterior
763 neighborhoods. I_a/I_p was calculated from the anterior and posterior *syg-1* bands on each
764 side of the embryonic nerve ring per embryo (number of embryos = 4, number of I_a/I_p
765 values = 8).

766

767 **Quantification of the dorsal midline shift (chiasm) length of AIB**

768 The dorsal midline shift (chiasm) lengths of AIB and AVE were calculated by
769 making 3D maximum intensity projections of confocal z-stacks and orienting the neuron
770 pair to a dorsal-ventral view. A straight line selection is made along the posterior-
771 anterior shift of each neuron, and each arm of the "X" of the chiasm was measured
772 (using Fiji).

773

774 **Quantification of distal neurite length of AIB**

775 The length of the distal neurite of AIB was measured by drawing a freehand line
776 along the neurite segment occupying the distal neighborhood (including the chiasm) in
777 maximum intensity projections of confocal image stacks where the worms are oriented
778 on their side (z-stacks acquired along left-right axis of the worm, producing a lateral
779 view of the neurons).

780

781 **Quantification of positions and velocities of the AIB neurite during**
782 **embryogenesis**

783 The positions of the AIB neurite in the anterior and posterior neighborhoods in Fig. 3C
784 are calculated from deconvolved maximum intensity projections of diSPIM images
785 where the neurons are oriented in an axial view. These positions are determined by
786 measuring the lengths along the AIB neurite from the unzippering/zippering forks to the
787 dorsal midline. The distance of the zippering fork from the midline is subtracted from the
788 total length of the neurite at the start of zippering, to obtain the length of the AIB neurite
789 that has already zippered. The fraction of the length of the AIB neurite that has zippered
790 to the initial length of the relocating AIB distal neurite, multiplied by 100, yields the
791 percentage of the AIB neurite that has zippered at each timepoint. The reported values
792 (in Fig. 5S) of the percentages of the AIB neurite that has zippered are averages across
793 the three independent embryo datasets (used for the Fig. 3 plots). Embryos in which the
794 AIB and RIM neurons were specifically labeled by the subtractive labeling strategy were

795 used for the analysis. Reported measurements represent AIB neurites which were
796 visible through the imaging window. Zippering velocity (Fig. 3D) at any timepoint (t1) is
797 defined as the difference between positions of the AIB neurite at that timepoint (t1) and
798 the next timepoint (t2) (for which position was measured), divided by the time interval
799 (t2-t1). These measurements are performed with CytoSHOW. To pseudocolor the
800 neurites for representation, we used the same steps described in **'Confocal imaging of**
801 ***C. elegans* larvae and image processing.'**

802

803 **Quantification of the angle of exit of the developing AIB distal neurite with the**
804 **ventral turn of the nerve ring in the posterior neighborhood**

805 The angle of exit (α) of the developing AIB distal neurite is measured as the
806 angle between straight line tangents drawn along the separating distal segment of AIBL
807 and the proximal neurite of AIBR and vice versa. These measurements are performed
808 on deconvolved maximum intensity projections of diSPIM images where the neurons
809 are oriented in an axial view. The angle of ventral turn of the nerve ring (β) is measured
810 as the angle between straight line tangents drawn along segments of the nerve ring on
811 either side of the ventral bend of the nerve ring in the posterior neighborhood (see
812 Supplementary Fig. 3G,H). β is measured from images of embryos with proximal
813 neighborhood labeled with *nphp-4* promoter (see Results and
814 http://promoters.wormguides.org). All measurements are performed using CytoSHOW.

815

816 **Imaging and representation of synaptic protein RAB-3 in AIB in embryos**

817 Time-lapse imaging of presynaptic protein RAB-3 in AIB in embryos was
818 performed using diSPIM (Wu et al., 2013). To visualize the distribution of RAB-3 along
819 the neurite we straightened the distal neurite of each AIB neuron from maximum
820 intensity projections where the AIB neurons are oriented in the axial view (Fig. 7).

821

822 **Quantification of nerve ring width from larval stage animals**

823 The nerve ring was visualized using a 5.6 kb promoter of *cnd-1* (Shah et al., 2017)
824 driving membrane-targeted GFP (PH:GFP) in wildtype and *syg-1(ky652)* mutant
825 animals. Measurements were done on confocal image stacks where the worms are
826 oriented on their side (z-stacks acquired along left-right axis of the worm, producing a
827 lateral view of the neurons). On each side of the worm a straight line selection along the
828 anterior-posterior axis from one edge of the labeled nerve ring to the other was defined
829 as the nerve ring width.

830

831 **Quantification of length of the dorsal midline shift (chiasm) from EM images**

832 From a segmented EM dataset of the L4 larva JSH (Brittin et al., 2018, White et
833 al., 1986), we calculated the number of z-slices containing segmented regions of the
834 anterior-posterior shift (that forms the chiasm) of AIBL. We multiplied this number with
835 the z-spacing of the dataset (60 nm) to obtain the anterior-posterior distance that the
836 AIBL shift spans (d_z). We then calculated the x-y distance between the segmented
837 regions of the AIBL shift in the topmost and bottommost z-slice(d_{x-y}). We calculate the
838 length of the shift in 3D (l) using the formula

839 $$\boldsymbol{l} = \sqrt{d_z^2 + d_{x-y}^2}$$

840 The same measurements were repeated for the length of the dorsal midline shift of
841 AIBR.

842

843 **Statistical analyses**

844 Statistical analyses were conducted with PRISM 7 software. For each case, the
845 chosen statistical test is described in the figure legend and "n" values are reported.
846 Briefly, for continuous data, comparisons between two groups were determined by
847 unpaired two-tailed t-test and comparisons within multiple groups were performed by
848 ordinary one-way ANOVA. Error bars were reported as standard error of the mean
849 (SEM). For categorical data, groups were compared with two-sided Fisher's exact test.
850 The range of p-values for significant differences are reported in the figure legend. The
851 Cohen's d statistic was determined for comparisons between continuous datasets with
852 statistically significant differences, to obtain estimates of effect sizes.

853

854 **Acknowledgements**

855 We thank Kang Shen, Harald Hutter and John Murray for providing strains and
856 constructs. We thank Scott Emmons, Steve Cook, and Chris Brittin, and Mei Zhen and
857 Daniel Witvliet for sharing their segmented EM data and adjacencies. We thank Thierry
858 Emonet and members of the Colón-Ramos lab for help, advice and insightful comments
859 during manuscript preparation. We thank Sarah Se-Hyun Jho and Kenya Collins for their

contributions to the project. We thank the Caenorhabditis Genetics Center (funded by NIH Office of Research Infrastructure Programs P40 OD010440) for *C. elegans* strains. We thank the Research Center for Minority Institutions program, the Marine Biological Laboratories (MBL), and the Instituto de Neurobiología de la Universidad de Puerto Rico for providing meeting and brainstorming platforms. H.S. and D.A.C-R. acknowledge the Whitman and Fellows program at MBL for providing funding and space for discussions valuable to this work. Research in the D.A.C-R., W.A.M., and Z. B. labs were supported by NIH grant No. R24-OD016474. M.W.M. was supported by NIH by F32-NS098616. Research in H.S. lab was further supported by the intramural research program of the National Institute of Biomedical Imaging and Bioengineering (NIBIB), NIH. Research in Z.B. lab was further supported by an NIH center grant to MSKCC (P30CA008748). Research in the D.A.C.-R. lab was further supported by NIH R01NS076558, DP1NS111778 and by an HHMI Scholar Award.

Author contributions

T.S. and D.A.C.-R. designed the experiments. T.S. performed the experiments and data analysis. X.H., Y.W. and H.S. designed and performed the triple-view confocal imaging and deep learning analysis. T.S., N.L.K., M.W.M., L.H.D., and N.V.-M. generated reagents and provided resources. T.S., N.L.K., M.W.M., L.S., Y.W., A.S., Z.B., H.S. and W.A.M developed, and designed methodologies used in the study. S.E.E. analyzed and interpreted embryonic transcriptomics data (Packer et al., 2019). L.F. and A.S. contributed lineaging data and expertise. T.S. and D.A.C.-R. prepared the manuscript with input from the other authors. Z.B., W.A.M., H.S., D.A.C.-R. supervised the project.

883

884 **Declaration of interests**

885 The authors declare no competing interests.

886

887 **Figure Legends**

888

889 **Fig. 1: AIB single neurite is placed along two distinct neighborhoods in the nerve**
890 **ring**

891

892 **A,** Schematic of an adult/larval *C. elegans* showing an AIB neuron (cyan) and its
893 posterior (orange) and anterior (magenta) neighborhoods in the head. The AIB neurite
894 has a proximal neurite segment (orange arrow), a posterior-anterior shift at the dorsal
895 midline (dashed line) and a distal neurite segment (magenta arrow; on the other side of
896 the worm, behind the pharynx, which is in gray). The neon-colored outline represents
897 the nerve ring neuropil. The terms 'proximal' or 'distal' neurite segments refer to the
898 relationship of the neurite segment to the AIB cell body. The neighborhoods in which the
899 'proximal' and 'distal' neurite segments are positioned are referred to as the 'posterior'
900 or 'anterior' neighborhoods, respectively, because of their position along the anterior-
901 posterior axis of the worm. Note that this schematic only shows one neuron of the AIB
902 pair. Cell body is marked with an asterisk.

903 **B,** Magnified schematic of AIB and its neighborhoods in **A**

904 **C,** Representative confocal image showing the lateral view of an AIB neuron labeled
905 with cytoplasmic mCherry (cyan).

906 **D,** Representative confocal image showing an AIB neuron labeled with cytoplasmic
907 mCherry (cyan); and RIM motor neuron of the anterior neighborhood labeled with
908 cytoplasmic GFP (magenta) in lateral view. Note the colocalization of the AIB distal
909 neurite (but not the proximal neurite) with the anterior neighborhood marker RIM
910 (compare with **E**).
911 **E,** As **D**, but with AIB (cyan) and AWC and ASE sensory neurons of the posterior
912 neighborhood (orange). Note the colocalization of the AIB proximal neurite (but not the
913 distal neurite) with the posterior neighborhood markers AWC and ASE (compare with
914 **D**).
915 **F-J,** Same as **A-E** but in axial view indicated by the arrow in **F**. Note shift in **H** (arrows),
916 corresponding to AIB neurite shifting neighborhoods (compare **I** and **J**).
917 **K,L,** Volumetric reconstruction from the JSH electron microscopy connectome dataset
918 (White et al., 1986) of AIBL (**K**), and AIBL overlaid on nerve ring strata **(L)**, in lateral
919 view, with S2 and S3 strata (named as in (Moyle et al., 2021)), containing anterior and
920 posterior neighborhoods, respectively.
921 **M,** Volumetric reconstruction of AIBL and AIBR in axial view (from the JSH dataset
922 (White et al., 1986)). Note the shift in neighborhoods by AIBL and AIBR, at the dorsal
923 midline (dashed line), forms a chiasm.
924 **N,** Schematic of **M,** highlighting the AIB neighborhoods for context and the dorsal
925 midline with a dashed line.
926 Scale bar = 10 μm for **A-J** and 3 μm for **K-N**.
927

928 **Fig. 2: A retrograde zippering mechanism positions the AIB neurites in the**
929 **anterior neighborhood during embryonic development**
930
931 **A,** Schematic of axial view of the AIB neuron pair: AIBL (cyan) and AIBR (yellow) in the
932 context of the nerve ring (light neon) and the pharynx (grey), with posterior
933 neighborhood labeled (orange) and the dashed line representing the dorsal midline
934 where the AIB chiasm is present in adults (see Fig. 1). Dotted box represents region in
935 **B'-F'**, and dotted box in **G.**
936 **B,F,** Time-lapse showing initial placement of AIBL and AIBR in the posterior
937 neighborhood and their subsequent separation from this neighborhood. Images are
938 deconvolved diSPIM maximum intensity projections obtained from developing embryos.
939 Neurons were individually pseudocolored to distinguish them (see Methods). The dorsal
940 half of the nerve ring (dotted box in **A**) are magnified in **B'-F'**. **B''-F''** are schematic
941 diagrams representing the images in **B-F**. Dashed vertical lines represent the dorsal
942 midline. Note in (**B, B', B''**), the AIBL and AIBR neurites approaching the dorsal midline
943 in the posterior neighborhood. In (**C, C', C''**), AIBL and AIBR have met at the dorsal
944 midline and continue growing along each other, past the midline. The latter part of the
945 neurite, past the midline, becomes the future distal neurite. (**D, D', D''**) shows the tip of
946 the AIBL future distal neurite moving away from the posterior neighborhood and its
947 counterpart, AIBR. The arrowhead indicates the point of separation of the AIBL distal
948 neurite and the AIBR proximal neurite. (**E, E', E''**) shows further separation of the two
949 neurites and by (**F, F', F''**), they have completely separated. The arrowheads in (**E, E',**
950 **E''**) and (**F, F', F''**) also indicate the junction between the separating AIBL distal neurite

951 and the AIBR proximal neurite. A similar sequence of events is visualized at higher
952 spatial resolution in Supplementary Fig. 3 using triple-view line scanning confocal
953 microscopy.

954 **G, G'**, Confocal micrograph of a postembryonic L4 animal (axial view) showing the
955 relationship between AIBL and AIBR. The region in the box represents the dorsal part of
956 the nerve ring, magnified in **G'**.

957 **H,** Axial view schematic of one AIB neuron (cyan) in the context of the anterior
958 neighborhood marker, the RIM neuron (magenta), the nerve ring (light neon) and the
959 pharynx (grey).

960 **I-K,** Time-lapse showing placement of the AIB neurite (cyan) relative to the anterior
961 neighborhood (magenta). As in **B-F**, images are deconvolved diSPIM maximum
962 intensity projections and the neurons were pseudocolored. The dorsal half of the nerve
963 ring (dotted box in **H**) are magnified in **I'-K'**. Dashed line indicates dorsal midline (where
964 the shift, or chiasm, in the adult is positioned, see Fig. 1). **I''-K''** are schematic diagrams
965 representing the images in **I-K**.

966 Note in (**I, I', I''**), the tip of the AIB neurite encounters the RIM neurite in the anterior
967 neighborhood (green arrowhead). In (**J, J', J''**), the AIB distal neurite has partially
968 aligned along the RIM neurites. The green arrowhead now indicates point of initial
969 encounter of the two neurites (same as in **I**'), and the red arrowhead indicates the
970 retrograde zippering event bringing the AIB and RIM neurons together in the anterior
971 neighborhood. In (**K, K', K''**) the two neurites have zippered up to the dorsal midline.
972 Arrow in **J'** indicates direction of zippering.

973 **L,** Confocal micrograph of a postembryonic L4 animal in axial view showing the final
974 position of AIB with respect to the anterior neighborhood. The same image as Fig. 1I
975 was used here for reference. The region in the dotted box represents dorsal part of the
976 nerve ring, magnified in (**L'**).
977 **M,** Schematic highlights the steps by which the AIB distal neurite is repositioned to a
978 new neighborhood – (i) exit from the posterior neighborhood and (ii) retrograde
979 zippering onto the anterior neighborhood with intermediate partially zippered states and
980 completely zippered states.
981 Scale bar = 10 μm for **B-G** and **I-L**.
982 Scale bar = 2 μm for **B'-G'** and **I'-L'**
983 Times are in m.p.f. (minutes post fertilization).
984
985 **Fig. 3: Biophysical modeling of AIB developmental dynamics is consistent with**
986 **differential adhesion leading to retrograde zippering**
987
988 **A,** Axial view schematic of a single AIB neuron during transition of its neurite between
989 the posterior (orange) and anterior (magenta) neighborhoods.
990 **B,B'** Magnified schematic of dotted inset in (**A**) showing the AIB neurite (cyan) during its
991 transition from the posterior to the anterior neighborhood. The lengths of the neurite
992 positioned in the posterior and anterior neighborhoods are denoted by L_p and L_a,
993 respectively. The velocity with which the AIB neurite zippers onto the anterior
994 neighborhood is denoted by v_{zip}, and the velocity with which it unzippers from the
995 posterior neighborhood is denoted by v_{unzip}. At the junction between the neurite and the

996 two neighborhoods, i.e., at the zippering and unzippering forks, tension and adhesion
997 forces act on the neurite (see **B'** and Supplementary Note 1). **B',** Schematic of AIB
998 neurite zippering to the anterior neighborhood. Adhesion $S_{anterior}$ acts in the direction of
999 zippering (and therefore in the direction of the zippering velocity v_{zip}), and favors
1000 zippering. Tension $T_{anterior}$ acts in the opposite direction, disfavoring zippering.
1001 **C,** Plot of position vs. time of the AIB neurite in both neighborhoods in synchronized
1002 embryos at the indicated timepoints on the x-axis (±5 mins). Plot shows mean of L_p
1003 (n=4) and L_a (n=3) values at different timepoints. Note zippering from the anterior
1004 neighborhood and unzippering from the posterior neighborhood take place in the same
1005 time window and are inversely related (between 500-545 m.p.f.). Quantifications were
1006 done from 3 embryos for each of L_a and L_p.
1007 **D,** Plot of zippering velocities vs time (n=3) for the indicated timepoints on the x-axis (±5
1008 mins). Note a tenfold increase in velocity mid-way through zippering (530 m.p.f.)
1009 m.p.f. = minutes post fertilization. Error bars represent standard error of the mean
1010 (S.E.M.), The three embryo datasets used for measuring L_a values in (**C**) were used to
1011 calculate zippering velocities.
1012 For **C** and **D**, n represents the number of AIB neurites quantified.
1013
1014 **Fig. 4: SYG-1 and SYG-2 are required for precise placement of the AIB neurite in**
1015 **the anterior neighborhood**
1016
1017 **A-D,** Representative confocal images of AIB (**A**) and RIM neurons (**B**) which mark the
1018 anterior neighborhood, in a wild type animal. (**C**) is a merge of **A** and **B**. The dashed

1019 box represents the region of contact of AIB with the anterior neighborhood, magnified in
1020 (**D**). The AIB distal neurite colocalizes extensively with the anterior neighborhood in wild
1021 type animals (Arrow in **D** and Supplementary Fig. 2A,B). Cell bodies are marked with an
1022 asterisk.

1023 **E-L,** As **A-D** but in the *syg-1(ky652)* (**E-H**) and *syg-2(ky671)* (**I-L**) mutant background.
1024 Note the gaps between the AIB distal neurite and the RIM neurites (**H,L**, arrows),
1025 indicating loss of contact between the AIB and the anterior neighborhood in these
1026 mutants.

1027 **M,** Schematic and scatter plot of quantifications of the loss of contacts between AIB and
1028 the anterior neighborhood for wild type (n=41), *syg-1(ky652)* mutant (n=39) and s*yg-*
1029 *2(ky671)* animals (n=49). 'n' represents the number of AIB neurites quantified from 21,
1030 20 and 25 animals respectively. The extent of detachment of the AIB distal neurite, and
1031 hence its deviation from the RIM neighborhood, was quantified using the indicated
1032 formula (see also Methods). Error bars indicate standard error of the mean (S.E.M.).
1033 ****$p<0.0001$, **$p=0.0095$ (one-way ANOVA with Dunnett's multiple comparisons test).
1034 n represents the number of AIB neurites quantified. Estimated effect size, d = 1.110 for
1035 WT vs. *syg-1(ky652)* and 0.775 for WT vs. *syg-2(ky671)*.

1036 **N,** Quantification of the penetrance of the AIB neurite placement defect as the
1037 percentage of animals with normal AIB distal neurite placement in WT, *syg-1(ky652),*
1038 *syg-2(ky671), syg-1(ky652);syg-2(ky671)* double mutant, *inx-1p:syg-2* rescue, *inx-*
1039 *1p:syg-1* rescue and SYG-1 cosmid rescue. *inx-1p* is a cell-specific promoter driving
1040 expression in AIB (Altun et al., 2008). The green and purple bars represent *syg-*
1041 *1(ky652)* and *syg-2(ky671)* mutant backgrounds respectively. Numbers on bars

1042 represent number of animals examined. ****p<0.0001 by two-sided Fisher's exact test
1043 between WT and *syg-1(ky652)*, between WT and *syg-2(ky671)*, and between *syg-*
1044 *1(ky652)* and SYG-1 cosmid rescue, and **p=0.0055 between *syg-2(ky671) and inx-*
1045 *1p:syg-2* rescue. There is no significant difference (abbreviated by n.s.) in penetrance
1046 between the *syg-1(ky652)* and *syg-1(ky652);syg-2(ky671)* (p=0.6000) populations and
1047 between *syg-1(ky652)* and the *inx-1p:syg-1* animals (p=0.3558).
1048 Scale bar = 10 μm, applies to **A-L.**
1049
1050 **Fig. 5: Increased local expression of SYG-1 in the anterior neighborhood**
1051 **coincides with zippering of the AIB neurite onto this neighborhood**
1052
1053 **A-E,** Schematic (**A**) and representative confocal image of a wild type animal co-
1054 expressing (**B**) a membrane-targeted *syg-1* transcriptional reporter (see Methods,
1055 (Schwarz et al., 2009)) and (**C**) cytoplasmic AIB reporter. Merged image in (**D**). Since
1056 the *syg-1* reporter is membrane-targeted, it labels cell body outlines and neurites (**B, D**).
1057 The dashed box or inset in (**D**) represents the region of overlap between AIB and *syg-1-*
1058 expressing neurites, magnified in (**E**). Note that the *syg-1* reporter shows two bands of
1059 expression in the nerve ring (arrows in **B** and **D**) which coincide with the posterior and
1060 anterior AIB neighborhoods (orange and magenta arrows). Note also that there is no
1061 membrane outline corresponding to the AIB cell body (**B,** we drew a dashed silhouette
1062 of the AIB cell body position as determined in **C**). Asterisk indicates cell body.
1063 **F-I,** As **B-E**, but with a translational SYG-1 reporter. Note the SYG-1 protein shows a
1064 similar expression pattern.

1065 **J-N,** Schematic (**J**) and time-lapse images (**K-N**) of SYG-1 translational reporter
1066 expression during embryogenesis (460-640 m.p.f.). Images are deconvolved diSPIM
1067 maximum intensity projections. The dashed boxes represent the dorsal half of the nerve
1068 ring and are magnified in **O-R**. **O'-R'** are schematic diagrams representing the images
1069 in **O-R**. In (**K, O, O'**), SYG-1 expression is primarily visible in a single band containing
1070 amphid neurites, and corresponding to the AIB posterior neighborhood. The magenta
1071 dashed line and magenta arrows point to the anterior neighborhood and the orange
1072 arrow, to the posterior neighborhood. By 535 m.p.f. (**L, P, P'**), SYG-1 expression is
1073 visible in both the anterior and posterior neighborhoods. In subsequent timepoints (**M,**
1074 **Q, Q', N, R, R'**), SYG-1 expression increases in the anterior neighborhood and
1075 decreases in the posterior neighborhood, coincident with AIB developmental events that
1076 enable its transition from the posterior to the anterior neighborhood (Fig. 2B-K). The
1077 *syg-1* transcriptional reporter shows a similar expression pattern throughout
1078 development (Supplementary Fig. 5).
1079 **S,** Plot showing relative enrichment of the *syg-1* transcriptional reporter in the anterior
1080 neighborhood over time (magenta) overlaid with plot showing percentage of the
1081 relocating AIB distal neurite that has zippered onto the anterior neighborhood (blue).
1082 Relative enrichment in the anterior neighborhood is defined as the ratio of mean
1083 intensity of the *syg-1* reporter in the band corresponding to the AIB anterior
1084 neighborhood, as compared to that in the posterior neighborhood (see Methods). This
1085 value is calculated starting at a timepoint when *syg-1* reporter expression becomes
1086 visible in the anterior neighborhood, and averaged for 4 embryos. The relative
1087 enrichment values plotted represent values calculated at the indicated developmental

1088 times on the x-axis (±10 mins). The reported values of "% AIB zippered" are averaged
1089 across the three independent embryo datasets used for the plots in Fig. 3. Note similar
1090 SYG-1 expression dynamics to zippering dynamics in AIB. Error bars represent
1091 standard error of the mean (S.E.M.).
1092 Scale bar = 10 μm, applies to **B-D**, **F-H** and **K-N**.
1093 Scale bar = 2 μm in **E, I,** and **O-R**
1094 Times are in m.p.f. (minutes post fertilization).
1095
1096 **Fig. 6: Ectopic *syg-1* expression is sufficient to alter placement of the AIB distal**
1097 **neurite**
1098
1099 **A,** Lateral view schematic of a wild type AIB neuron (cyan) in the context of the
1100 posterior (orange) and anterior (magenta) neighborhoods, and the nerve ring (light
1101 neon). Higher SYG-1 endogenous expression in the anterior neighborhood represented
1102 by yellow arrowhead.
1103 **B-C,** Confocal image of a wild type animal with AIB (labeled with cytoplasmic mCherry,
1104 in cyan) and the posterior neighborhood neurons AWC and ASE (labeled with
1105 cytoplasmic GFP, in orange). The dashed box represents the region of contact between
1106 AIB and the posterior neighborhood neurons, magnified in (**C**).
1107 **D-F,** As (**A-C**), but in the *syg-1(ky652)* lof (loss of function) mutant background. Note
1108 that the distal neurite is positioned away from the posterior neighborhood, as in wild
1109 type, although these animals display defects in fasciculation with the anterior
1110 neighborhood (as shown in Fig. 4).

1111 **G-I,** As (**D-F**), but with ectopic overexpression of SYG-1 in the posterior neighborhood
1112 neurons. In the schematic (**G**), expression of SYG-1 in the posterior neighborhood
1113 (achieved here using *nphp-4p*, also see Supplementary Fig. 8A,B) is represented by a
1114 yellow arrowhead (as in (**A**), but here in posterior neighborhood). Note that the AIB
1115 distal neurite is now abnormally positioned in the posterior neighborhood in which SYG-
1116 1 was ectopically expressed (**H, I**).
1117 **J,** Schematic (left) and scatter plot quantification (right) of minimum perpendicular
1118 distances (d_{min}, indicated by black double-headed arrow) between the AIB distal neurite
1119 and posterior neighborhood neurons in WT (in black, n=17), *syg-1(ky652)* (in green,
1120 n=18), and two *syg-1(ky652)* populations with SYG-1 overexpressed in two different
1121 sets of posterior neighborhood neurons via the use of *nphp-4p* and (in blue) *mgl-1bp* (in
1122 red) (n=18 and n=16 respectively). **p= 0.0056 and 0.0070 respectively (one-way
1123 ANOVA with Dunnett's multiple comparisons test). Effect size estimate, d = 1.075 and
1124 1.140 respectively. Error bars indicate standard error of the mean (S.E.M.). n represents
1125 the number of AIB neurites quantified. Quantifications were done from 9 animals each
1126 for WT, *syg-1(ky652)* and nphp-4:syg-1; *syg-1(ky652)* and 8 animals for mgl-1b:syg-1;
1127 *syg-1(ky652)*.
1128 **K,** Quantification of penetrance of the ectopic AIB neurite placement represented as the
1129 percentage of animals with the AIB distal neurite partially positioned in the posterior
1130 neighborhood in the WT, *syg-1(ky652)* and posterior SYG-1 overexpression strains
1131 (colors represent the same strains as in **J**). Numbers on bars represent number of
1132 animals examined. ***p=0.0002 for *syg-1(ky652)* and *nphp-4p* expressed SYG-1 and

1133 ****p<0.0001 for *syg-1(ky652)* and *mgl-1bp* expressed SYG-1 by two-sided Fisher's
1134 exact test.
1135 Scale bar = 10 μm in **B**, **E** and **H** and 1 μm in **C**, **F**, and **I**. Cell body is marked with an
1136 asterisk.
1137
1138 **Fig. 7: AIB neurite placement by retrograde zippering, and presynaptic assembly**
1139 **are coordinated during development**
1140
1141 **A,** Axial view schematic of the AIB neurons (cyan) with presynaptic protein RAB-3
1142 (yellow) puncta along the distal neurite. Arrowhead indicates the tip of the distal neurite
1143 and arrow/dashed line indicate the dorsal midline.
1144 **B-E,** Time-lapse imaging of RAB-3 localization in AIB during embryogenesis. **B-E** are
1145 merged diSPIM maximum intensity projections of AIB labeled with membrane-tagged
1146 mCherry (cyan) and AIB presynaptic sites labeled with GFP:RAB-3 (yellow), at different
1147 timepoints during embryogenesis. **B'-E'** represent the GFP:RAB-3 channel for images
1148 in **B-E**. Note in (**B, B'**) and (**C, C'**) that the RAB-3 signal in the neurite is localized
1149 exclusively near the neurite tip. As development progresses, there is more RAB-3 signal
1150 throughout the neurite from the tip up to the midline (in (**D, D'**) and (**E, E'**)). Therefore,
1151 RAB-3 becomes progressively enriched from the tip up to the midline during
1152 development, and the timing for this process correlates, with a slight delay, with the
1153 developmental timing of AIB zippering (Fig. 2I-K). Arrowhead and arrow, as in (**A**),
1154 indicate the tip of the distal neurite and the region of the neurite near the dorsal midline
1155 (dashed vertical line) respectively. Scale bar = 10 μm applies (**B-E**) and (**B'-E'**).

1156 **F-I,** Straightened distal neurites from AIB (corresponding to the region in (**B-E**) which is
1157 marked by the arrowhead (AIB tip) and arrows (dorsal midline). Note presynaptic
1158 assembly, as imaged by RAB-3 accumulation, from the tip of the neurite towards the
1159 midline of AIB, reminiscent of the zippering event (Fig. 2). Scale bar = 1 μm applies **F-I**.
1160 **J,** Schematic model showing progressive retrograde zippering leading to placement of
1161 the AIB neurite along two different layers. This is accompanied by a switch in SYG-1
1162 expression between layers, and synaptic protein localization in a retrograde order along
1163 the neurite, resembling the order of zippering.
1164
1165

1166 **References**

1167

1168 ALTUN, Z. F., CHEN, B., WANG, Z. W. & HALL, D. H. 2008. High resolution map of
1169 Caenorhabditis elegans gap junction proteins. *Developmental Dynamics*.
1170 ARMENTI, S. T., LOHMER, L. L., SHERWOOD, D. R. & NANCE, J. 2014. Repurposing
1171 an endogenous degradation system for rapid and targeted depletion of C.
1172 elegans proteins. *Development (Cambridge)*.
1173 AURELIO, O., BOULIN, T. & HOBERT, O. 2003. Identification of spatial and temporal
1174 cues that regulate postembryonic expression of axon maintenance factors in the
1175 C. elegans ventral nerve cord. *Development,* 130**,** 599-610.
1176 BAIER, H. 2013. Synaptic laminae in the visual system: Molecular mechanisms forming
1177 layers of perception.
1178 BAO, S. & CAGAN, R. 2005. Preferential adhesion mediated by Hibris and Roughest
1179 regulates morphogenesis and patterning in the Drosophila eye. *Dev Cell,* 8**,** 925-
1180 35.
1181 BAO, S., FISCHBACH, K. F., CORBIN, V. & CAGAN, R. L. 2010. Preferential adhesion
1182 maintains separation of ommatidia in the Drosophila eye. *Dev Biol,* 344**,** 948-56.
1183 BAO, Z., MURRAY, J. I., BOYLE, T., OOI, S. L., SANDEL, M. J. & WATERSTON, R. H.
1184 2006. Automated cell lineage tracing in Caenorhabditis elegans. *Proceedings of*
1185 *the National Academy of Sciences of the United States of America*.
1186 BARRY, J., GU, Y. & GU, C. 2010. Polarized targeting of L1-CAM regulates axonal and
1187 dendritic bundling in vitro. *European Journal of Neuroscience*.
1188 BOYLE, T. J., BAO, Z., MURRAY, J. I., ARAYA, C. L. & WATERSTON, R. H. 2006.
1189 AceTree: a tool for visual analysis of Caenorhabditis elegans embryogenesis.
1190 *BMC Bioinformatics,* 7**,** 275.

BRITTIN, C., COOK, S., HALL, D., EMMONS, S. & COHEN, N. 2018. Volumetric reconstruction of main Caenorhabditis elegans neuropil at two different time points. *bioRxiv*.

BRITTIN, C. A., COOK, S. J., HALL, D. H., EMMONS, S. W. & COHEN, N. 2021. A multi-scale brain map derived from whole-brain volumetric reconstructions. *Nature,* 591**,** 105-110.

CANTY, L., ZAROUR, E., KASHKOOLI, L., FRANÇOIS, P. & FAGOTTO, F. 2017. Sorting at embryonic boundaries requires high heterotypic interfacial tension. *Nature Communications,* 8**,** 157.

CHAO, D. L. & SHEN, K. 2008. Functional dissection of SYG-1 and SYG-2, cell adhesion molecules required for selective synaptogenesis in C. elegans. *Mol Cell Neurosci,* 39**,** 248-57.

CHELUR, D. S. & CHALFIE, M. 2007. Targeted cell killing by reconstituted caspases. *Proc Natl Acad Sci U S A,* 104**,** 2283-8.

COOK, S. J., JARRELL, T. A., BRITTIN, C. A., WANG, Y., BLONIARZ, A. E., YAKOVLEV, M. A., NGUYEN, K. C. Q., TANG, L. T. H., BAYER, E. A., DUERR, J. S., BÜLOW, H. E., HOBERT, O., HALL, D. H. & EMMONS, S. W. 2019. Whole-animal connectomes of both Caenorhabditis elegans sexes. *Nature*.

DAVIS, M. W., HAMMARLUND, M., HARRACH, T., HULLETT, P., OLSEN, S. & JORGENSEN, E. M. 2005. Rapid single nucleotide polymophism mapping in C. elegans. *BMC Genomics*.

DEMB, J. B. & SINGER, J. H. 2012. Intrinsic properties and functional circuitry of the AII amacrine cell.

DUAN, X., KRISHNASWAMY, A., DE LA HUERTA, I. & SANES, J. R. 2014. Type II cadherins guide assembly of a direction-selective retinal circuit. *Cell,* 158**,** 793-807.

DUGUAY, D., FOTY, R. A. & STEINBERG, M. S. 2003. Cadherin-mediated cell adhesion and tissue segregation: qualitative and quantitative determinants. *Developmental Biology,* 253**,** 309-323.

DUNCAN, L. H., MOYLE, M. W., SHAO, L., SENGUPTA, T., IKEGAMI, R., KUMAR, A., GUO, M., CHRISTENSEN, R., SANTELLA, A., BAO, Z., SHROFF, H., MOHLER, W. & COLÓN-RAMOS, D. A. 2019. Isotropic light-sheet microscopy and automated cell lineage analyses to catalogue caenorhabditis elegans embryogenesis with subcellular resolution. *Journal of Visualized Experiments*.

DWORAK, H. A., CHARLES, M. A., PELLERANO, L. B. & SINK, H. 2001. Characterization of Drosophila hibris, a gene related to human nephrin. *Development,* 128**,** 4265-76.

ERZBERGER, A., JACOBO, A., DASGUPTA, A. & HUDSPETH, A. J. 2020. Mechanochemical symmetry breaking during morphogenesis of lateral-line sensory organs. *Nat Phys,* 16**,** 949-957.

FORNITO, A., ZALESKY, A. & BULLMORE, E. T. 2016. *Fundamentals of brain network analysis,* Amsterdam ; Boston, Elsevier/Academic Press.

FOTY, R. A., PFLEGER, C. M., FORGACS, G. & STEINBERG, M. S. 1996. Surface tensions of embryonic tissues predict their mutual envelopment behavior. *Development,* 122**,** 1611-1620.

FOTY, R. A. & STEINBERG, M. S. 2005. The differential adhesion hypothesis: A direct evaluation. *Developmental Biology*.

FOTY, R. A. & STEINBERG, M. S. 2013. Differential adhesion in model systems.

GABRIEL, JENS P., TRIVEDI, CHINTAN A., MAURER, COLETTE M., RYU, S. & BOLLMANN, JOHANN H. 2012. Layer-Specific Targeting of Direction-Selective Neurons in the Zebrafish Optic Tectum. *Neuron,* 76**,** 1147-1160.

GALLETTA, B. J., CHAKRAVARTI, M., BANERJEE, R. & ABMAYR, S. M. 2004. SNS: Adhesive properties, localization requirements and ectodomain dependence in S2 cells and embryonic myoblasts. *Mech Dev,* 121**,** 1455-68.

GARG, P., VERMA, R., NIHALANI, D., JOHNSTONE, D. B. & HOLZMAN, L. B. 2007. Neph1 Cooperates with Nephrin To Transduce a Signal That Induces Actin Polymerization. *Molecular and Cellular Biology*.

GERKE, P., HUBER, T. B., SELLIN, L., BENZING, T. & WALZ, G. 2003. Homodimerization and heterodimerization of the glomerular podocyte proteins nephrin and NEPH1. *J Am Soc Nephrol,* 14**,** 918-26.

GODT, D. & TEPASS, U. 1998. Drosophila oocyte localization is mediated by differential cadherin-based adhesion. *Nature,* 395**,** 387-391.

GONZALEZ-REYES, A. & ST JOHNSTON, D. 1998. The Drosophila AP axis is polarised by the cadherin-mediated positioning of the oocyte. *Development,* 125**,** 3635-3644.

GREER, E. R., PEREZ, C. L., VAN GILST, M. R., LEE, B. H. & ASHRAFI, K. 2008. Neural and molecular dissection of a C. elegans sensory circuit that regulates fat and feeding. *Cell Metab,* 8**,** 118-31.

HAN, J., KAMBER, M. & PEI, J. 2012. 2 - Getting to Know Your Data. *In:* HAN, J., KAMBER, M. & PEI, J. (eds.) *Data Mining (Third Edition).* Boston: Morgan Kaufmann.

JONTES, J. D., BUCHANAN, J. & SMITH, S. J. 2000. Growth cone and dendrite dynamics in zebrafish embryos: early events in synaptogenesis imaged in vivo. *Nat Neurosci,* 3**,** 231-7.

KATZ, M. J. 1985. How straight do axons grow? *The Journal of Neuroscience,* 5**,** 589.

KIM, B. & EMMONS, S. W. 2017. Multiple conserved cell adhesion protein interactions mediate neural wiring of a sensory circuit in C. elegans. *Elife,* 6.

KIM, K., KIM, R. & SENGUPTA, P. 2010. The HMX/NKX homeodomain protein MLS-2 specifies the identity of the AWC sensory neuron type via regulation of the ceh-36 Otx gene in C. elegans. *Development,* 137**,** 963-74.

KOESTINGER, G., MARTIN, K. A. C., ROTH, S. & RUSCH, E. S. 2017. Synaptic connections formed by patchy projections of pyramidal cells in the superficial layers of cat visual cortex. *Brain Struct Funct,* 222**,** 3025-3042.

KOLB, H. 1995. *Roles of Amacrine Cells*.

KOLODKIN, A. L. & HIESINGER, P. R. 2017. Wiring visual systems: common and divergent mechanisms and principles. *Curr Opin Neurobiol,* 42**,** 128-135.

KRIEG, M., ARBOLEDA-ESTUDILLO, Y., PUECH, P. H., KAFER, J., GRANER, F., MULLER, D. J. & HEISENBERG, C. P. 2008. Tensile forces govern germ-layer organization in zebrafish. *Nat Cell Biol,* 10**,** 429-36.

KUMAR, A., WU, Y., CHRISTENSEN, R., CHANDRIS, P., GANDLER, W., MCCREEDY, E., BOKINSKY, A., COLÓN-RAMOS, D. A., BAO, Z., MCAULIFFE,

M., RONDEAU, G. & SHROFF, H. 2014. Dual-view plane illumination microscopy for rapid and spatially isotropic imaging. *Nature Protocols*.

KUNZEVITZKY, N. J., WILLEFORD, K. T., FEUER, W. J., ALMEIDA, M. V. & GOLDBERG, J. L. 2013. Amacrine cell subtypes differ in their intrinsic neurite growth capacity. *Investigative Ophthalmology and Visual Science*.

KURAMOCHI, M. & DOI, M. 2019. An Excitatory/Inhibitory Switch From Asymmetric Sensory Neurons Defines Postsynaptic Tuning for a Rapid Response to NaCl in Caenorhabditis elegans. *Frontiers in Molecular Neuroscience,* 11**,** 484.

LIN, D. M., FETTER, R. D., KOPCZYNSKI, C., GRENNINGLOH, G. & GOODMAN, C. S. 1994. Genetic analysis of Fasciclin II in Drosophila: defasciculation, refasciculation, and altered fasciculation. *Neuron,* 13**,** 1055-69.

MARC, R. E., ANDERSON, J. R., JONES, B. W., SIGULINSKY, C. L. & LAURITZEN, J. S. 2014. The AII amacrine cell connectome: a dense network hub. *Front Neural Circuits,* 8**,** 104.

MAYNARD, D. M. 1962. Organization of Neuropil. *Am. Zoologist***,** 79-96.

MELLO, C. & FIRE, A. 1995. DNA Transformation. *Methods in Cell Biology*.

MILLARD, S. S. & PECOT, M. Y. 2018. Strategies for assembling columns and layers in the Drosophila visual system. *Neural Dev,* 13**,** 11.

MINEVICH, G., PARK, D. S., BLANKENBERG, D., POOLE, R. J. & HOBERT, O. 2012. CloudMap: A cloud-based pipeline for analysis of mutant genome sequences. *Genetics*.

MISSAIRE, M. & HINDGES, R. 2015. The role of cell adhesion molecules in visual circuit formation: from neurite outgrowth to maps and synaptic specificity. *Dev Neurobiol,* 75**,** 569-83.

MISSLER, M., SUDHOF, T. C. & BIEDERER, T. 2012. Synaptic cell adhesion. *Cold Spring Harb Perspect Biol,* 4**,** a005694.

MOYLE, M. W., BARNES, K. M., KUCHROO, M., GONOPOLSKIY, A., DUNCAN, L. H., SENGUPTA, T., SHAO, L., GUO, M., SANTELLA, A., CHRISTENSEN, R., KUMAR, A., WU, Y., MOON, K. R., WOLF, G., KRISHNASWAMY, S., BAO, Z., SHROFF, H., MOHLER, W. A. & COLON-RAMOS, D. A. 2021. Structural and developmental principles of neuropil assembly in C. elegans. *Nature,* 591**,** 99-104.

MURRAY, J. I., BAO, Z., BOYLE, T. J. & WATERSTON, R. H. 2006. The lineaging of fluorescently-labeled Caenorhabditis elegans embryos with StarryNite and AceTree. *Nat Protoc,* 1**,** 1468-76.

NEUMANN-HAEFELIN, E., KRAMER-ZUCKER, A., SLANCHEV, K., HARTLEBEN, B., NOUTSOU, F., MARTIN, K., WANNER, N., RITTER, A., GODEL, M., PAGEL, P., FU, X., MULLER, A., BAUMEISTER, R., WALZ, G. & HUBER, T. B. 2010. A model organism approach: defining the role of Neph proteins as regulators of neuron and kidney morphogenesis. *Hum Mol Genet,* 19**,** 2347-59.

NEVIN, L. M., TAYLOR, M. R. & BAIER, H. 2008. Hardwiring of fine synaptic layers in the zebrafish visual pathway. *Neural Development*.

NGUYEN-BA-CHARVET, K. T. & CHEDOTAL, A. 2014. Development of retinal layers. *C R Biol,* 337**,** 153-9.

OZKAN, E., CHIA, P. H., WANG, R. R., GORIATCHEVA, N., BOREK, D., OTWINOWSKI, Z., WALZ, T., SHEN, K. & GARCIA, K. C. 2014. Extracellular

architecture of the SYG-1/SYG-2 adhesion complex instructs synaptogenesis. *Cell,* 156**,** 482-94.

OZTOKATLI, H., HORNBERG, M., BERGHARD, A. & BOHM, S. 2012. Retinoic acid receptor and CNGA2 channel signaling are part of a regulatory feedback loop controlling axonal convergence and survival of olfactory sensory neurons. *FASEB J,* 26**,** 617-27.

PACKER, J. S., ZHU, Q., HUYNH, C., SIVARAMAKRISHNAN, P., PRESTON, E., DUECK, H., STEFANIK, D., TAN, K., TRAPNELL, C., KIM, J., WATERSTON, R. H. & MURRAY, J. I. 2019. A lineage-resolved molecular atlas of C. elegans embryogenesis at single-cell resolution. *Science,* 365.

PETROVIC, M. & HUMMEL, T. 2008. Temporal identity in axonal target layer recognition. *Nature*.

PIGGOTT, B. J., LIU, J., FENG, Z., WESCOTT, S. A. & XU, X. Z. S. 2011. The neural circuits and synaptic mechanisms underlying motor initiation in C. elegans. *Cell*.

POSKANZER, K., NEEDLEMAN, L. A., BOZDAGI, O. & HUNTLEY, G. W. 2003. N-cadherin regulates ingrowth and laminar targeting of thalamocortical axons. *The Journal of neuroscience : the official journal of the Society for Neuroscience*.

PRICE, S. R., DE MARCO GARCIA, N. V., RANSCHT, B. & JESSELL, T. M. 2002. Regulation of motor neuron pool sorting by differential expression of type II cadherins. *Cell,* 109**,** 205-16.

ROBLES, E., FILOSA, A. & BAIER, H. 2013. Precise lamination of retinal axons generates multiple parallel input pathways in the tectum. *Journal of Neuroscience*.

RUBINOV, M. & SPORNS, O. 2010. Complex network measures of brain connectivity: Uses and interpretations. *NeuroImage*.

SABRIN, K., WEI, Y., VAN DEN HEUVEL, M. & DOVROLIS, C. 2019. The hourglass organization of the Caenorhabditis elegans connectome. *bioRxiv*.

SANES, J. R. & ZIPURSKY, S. L. 2010. Design principles of insect and vertebrate visual systems. *Neuron,* 66**,** 15-36.

SANES, J. R. & ZIPURSKY, S. L. 2020. Synaptic Specificity, Recognition Molecules, and Assembly of Neural Circuits.

SARIN, S., PRABHU, S., O'MEARA, M. M., PE'ER, I. & HOBERT, O. 2008. Caenorhabditis elegans mutant allele identification by whole-genome sequencing. *Nature Methods*.

SCHINDELIN, J., ARGANDA-CARRERAS, I., FRISE, E., KAYNIG, V., LONGAIR, M., PIETZSCH, T., PREIBISCH, S., RUEDEN, C., SAALFELD, S., SCHMID, B., TINEVEZ, J. Y., WHITE, D. J., HARTENSTEIN, V., ELICEIRI, K., TOMANCAK, P. & CARDONA, A. 2012. Fiji: an open-source platform for biological-image analysis. *Nat Methods,* 9**,** 676-82.

SCHOTZ, E. M., BURDINE, R. D., JULICHER, F., STEINBERG, M. S., HEISENBERG, C. P. & FOTY, R. A. 2008. Quantitative differences in tissue surface tension influence zebrafish germ layer positioning. *HFSP J,* 2**,** 42-56.

SCHÜRMANN, F. W. 2016. Fine structure of synaptic sites and circuits in mushroom bodies of insect brains.

SCHWABE, T., BORYCZ, J. A., MEINERTZHAGEN, I. A. & CLANDININ, T. R. 2019. Differential Adhesion Determines the Organization of Synaptic Fascicles in the Drosophila Visual System. *Curr Biol,* 29**,** 715.

SCHWARZ, V., PAN, J., VOLTMER-IRSCH, S. & HUTTER, H. 2009. IgCAMs redundantly control axon navigation in Caenorhabditis elegans. *Neural Development*.

SERIZAWA, S., MIYAMICHI, K., TAKEUCHI, H., YAMAGISHI, Y., SUZUKI, M. & SAKANO, H. 2006. A Neuronal Identity Code for the Odorant Receptor-Specific and Activity-Dependent Axon Sorting. *Cell*.

SHAH, P. K., TANNER, M. R., KOVACEVIC, I., RANKIN, A., MARSHALL, T. E., NOBLETT, N., TRAN, N. N., ROENSPIES, T., HUNG, J., CHEN, Z., SLATCULESCU, C., PERKINS, T. J., BAO, Z. & COLAVITA, A. 2017. PCP and SAX-3/Robo Pathways Cooperate to Regulate Convergent Extension-Based Nerve Cord Assembly in C. elegans. *Developmental cell,* 41**,** 195-203.e3.

SHEN, K. & BARGMANN, C. I. 2003. The immunoglobulin superfamily protein SYG-1 determines the location of specific synapses in C. elegans. *Cell,* 112**,** 619-30.

SHEN, K., FETTER, R. D. & BARGMANN, C. I. 2004. Synaptic specificity is generated by the synaptic guidepost protein SYG-2 and its receptor, SYG-1. *Cell*.

SMIT, D., FOUQUET, C., PINCET, F., ZAPOTOCKY, M. & TREMBLEAU, A. 2017. Axon tension regulates fasciculation/defasciculation through the control of axon shaft zippering. *Elife,* 6.

SOIZA-REILLY, M. & COMMONS, K. G. 2014. Unraveling the architecture of the dorsal raphe synaptic neuropil using high-resolution neuroanatomy. *Front Neural Circuits,* 8**,** 105.

STEINBERG, M. S. 1962. Mechanism of tissue reconstruction by dissociated cells, II: Time-course of events. *Science*.

STEINBERG, M. S. 1963. Reconstruction of tissues by dissociated cells. Some morphogenetic tissue movements and the sorting out of embryonic cells may have a common explanation. *Science,* 141**,** 401-8.

STEINBERG, M. S. 1970. Does differential adhesion govern self-assembly processes in histogenesis? Equilibrium configurations and the emergence of a hierarchy among populations of embryonic cells. *Journal of Experimental Zoology,* 173**,** 395-433.

STEINBERG, M. S. & GILBERT, S. F. 2004. Townes and Holtfreter (1955): directed movements and selective adhesion of embryonic amphibian cells. *J Exp Zool A Comp Exp Biol,* 301**,** 701-6.

STEINBERG, M. S. & TAKEICHI, M. 1994. Experimental specification of cell sorting, tissue spreading, and specific spatial patterning by quantitative differences in cadherin expression. *Proc Natl Acad Sci U S A,* 91**,** 206-9.

STRETTOI, E., RAVIOLA, E. & DACHEUX, R. F. 1992. Synaptic connections of the narrow‐field, bistratified rod amacrine cell (AII) in the rabbit retina. *Journal of Comparative Neurology*.

STRUNKELNBERG, M., BONENGEL, B., MODA, L. M., HERTENSTEIN, A., DE COUET, H. G., RAMOS, R. G. & FISCHBACH, K. F. 2001. rst and its paralogue kirre act redundantly during embryonic muscle development in Drosophila. *Development,* 128**,** 4229-39.

TAN, L., ZHANG, K. X., PECOT, M. Y., NAGARKAR-JAISWAL, S., LEE, P. T., TAKEMURA, S. Y., MCEWEN, J. M., NERN, A., XU, S., TADROS, W., CHEN, Z., ZINN, K., BELLEN, H. J., MOREY, M. & ZIPURSKY, S. L. 2015. Ig Superfamily Ligand and Receptor Pairs Expressed in Synaptic Partners in Drosophila. *Cell*.

TAYLOR, W. R. & SMITH, R. G. 2012. The role of starburst amacrine cells in visual signal processing. *Visual Neuroscience*.

TESSIER-LAVIGNE, M. & GOODMAN, C. S. 1996. The molecular biology of axon guidance. *Science,* 274**,** 1123-33.

TOWLSON, E. K., VÉRTES, P. E., AHNERT, S. E., SCHAFER, W. R. & BULLMORE, E. T. 2013. The rich club of the C. elegans neuronal connectome. *Journal of Neuroscience*.

VOYIADJIS, A. G., DOUMI, M., CURCIO, E. & SHINBROT, T. 2011. Fasciculation and defasciculation of neurite bundles on micropatterned substrates. *Annals of Biomedical Engineering*.

WEIGERT, M., SCHMIDT, U., BOOTHE, T., MÜLLER, A., DIBROV, A., JAIN, A., WILHELM, B., SCHMIDT, D., BROADDUS, C., CULLEY, S., ROCHA-MARTINS, M., SEGOVIA-MIRANDA, F., NORDEN, C., HENRIQUES, R., ZERIAL, M., SOLIMENA, M., RINK, J., TOMANCAK, P., ROYER, L., JUG, F. & MYERS, E. W. 2018. Content-aware image restoration: pushing the limits of fluorescence microscopy. *Nature Methods*.

WHITE, J. G., SOUTHGATE, E., THOMSON, J. N. & BRENNER, S. 1983. Factors that determine connectivity in the nervous system of Caenorhabditis elegans. *Cold Spring Harbor symposia on quantitative biology*.

WHITE, J. G., SOUTHGATE, E., THOMSON, J. N. & BRENNER, S. 1986. The structure of the nervous system of the nematode Caenorhabditis elegans. *Philos Trans R Soc Lond B Biol Sci,* 314**,** 1-340.

WITVLIET, D., MULCAHY, B., MITCHELL, J. K., MEIROVITCH, Y., BERGER, D. R., WU, Y., LIU, Y., KOH, W. X., PARVATHALA, R., HOLMYARD, D., SCHALEK, R. L., SHAVIT, N., CHISHOLM, A. D., LICHTMAN, J. W., SAMUEL, A. D. T. & ZHEN, M. 2020. Connectomes across development reveal principles of brain maturation in C. elegans. *bioRxiv***,** 2020.04.30.066209-2020.04.30.066209.

WU, Y., CHANDRIS, P., WINTER, P. W., KIM, E. Y., JAUMOUILLÉ, V., KUMAR, A., GUO, M., LEUNG, J. M., SMITH, C., REY-SUAREZ, I., LIU, H., WATERMAN, C. M., RAMAMURTHI, K. S., LA RIVIERE, P. J. & SHROFF, H. 2016. Simultaneous multiview capture and fusion improves spatial resolution in wide-field and light-sheet microscopy. *Optica*.

WU, Y., GHITANI, A., CHRISTENSEN, R., SANTELLA, A., DU, Z., RONDEAU, G., BAO, Z., COLON-RAMOS, D. & SHROFF, H. 2011. Inverted selective plane illumination microscopy (iSPIM) enables coupled cell identity lineaging and neurodevelopmental imaging in Caenorhabditis elegans. *Proc Natl Acad Sci U S A,* 108**,** 17708-13.

WU, Y., WAWRZUSIN, P., SENSENEY, J., FISCHER, R. S., CHRISTENSEN, R., SANTELLA, A., YORK, A. G., WINTER, P. W., WATERMAN, C. M., BAO, Z., COLÓN-RAMOS, D. A., MCAULIFFE, M. & SHROFF, H. 2013. Spatially isotropic

four-dimensional imaging with dual-view plane illumination microscopy. *Nature Biotechnology*.

XIE, X., TABUCHI, M., BROWN, M. P., MITCHELL, S. P., WU, M. N. & KOLODKIN, A. L. 2017. The laminar organization of the Drosophila ellipsoid body is semaphorin-dependent and prevents the formation of ectopic synaptic connections. *Elife,* 6.

XU, C. S., JANUSZEWSKI, M., LU, Z., TAKEMURA, S.-Y., HAYWORTH, K. J., HUANG, G., SHINOMIYA, K., MAITIN-SHEPARD, J., ACKERMAN, D., BERG, S., BLAKELY, T., BOGOVIC, J., CLEMENTS, J., DOLAFI, T., HUBBARD, P., KAINMUELLER, D., KATZ, W., KAWASE, T., KHAIRY, K. A., LEAVITT, L., LI, P. H., LINDSEY, L., NEUBARTH, N., OLBRIS, D. J., OTSUNA, H., TROUTMAN, E. T., UMAYAM, L., ZHAO, T., ITO, M., GOLDAMMER, J., WOLFF, T., SVIRSKAS, R., SCHLEGEL, P., NEACE, E. R., KNECHT, C. J., ALVARADO, C. X., BAILEY, D. A., BALLINGER, S., BORYCZ, J. A., CANINO, B. S., CHEATHAM, N., COOK, M., DREHER, M., DUCLOS, O., EUBANKS, B., FAIRBANKS, K., FINLEY, S., FORKNALL, N., FRANCIS, A., HOPKINS, G. P., JOYCE, E. M., KIM, S., KIRK, N. A., KOVALYAK, J., LAUCHIE, S. A., LOHFF, A., MALDONADO, C., MANLEY, E. A., MCLIN, S., MOONEY, C., NDAMA, M., OGUNDEYI, O., OKEOMA, N., ORDISH, C., PADILLA, N., PATRICK, C., PATERSON, T., PHILLIPS, E. E., PHILLIPS, E. M., RAMPALLY, N., RIBEIRO, C., ROBERTSON, M. K., RYMER, J. T., RYAN, S. M., SAMMONS, M., SCOTT, A. K., SCOTT, A. L., SHINOMIYA, A., SMITH, C., SMITH, K., SMITH, N. L., SOBESKI, M. A., SULEIMAN, A., SWIFT, J., TAKEMURA, S., TALEBI, I., TARNOGORSKA, D., TENSHAW, E., TOKHI, T., WALSH, J. J., YANG, T., HORNE, J. A., LI, F., PAREKH, R., RIVLIN, P. K., JAYARAMAN, V., ITO, K., SAALFELD, S., GEORGE, R., MEINERTZHAGEN, I., et al. 2020. A Connectome of the Adult Drosophila Central Brain. *bioRxiv***,** 2020.01.21.911859-2020.01.21.911859.

YAMAGATA, M. & SANES, J. R. 2008. Dscam and Sidekick proteins direct lamina-specific synaptic connections in vertebrate retina. *Nature*.

YAMAGATA, M. & SANES, J. R. 2012. Expanding the Ig superfamily code for laminar specificity in retina: Expression and role of contactins. *Journal of Neuroscience*.

YIP, Z. C. & HEIMAN, M. G. 2018. Ordered arrangement of dendrites within a C. elegans sensory nerve bundle. *Elife,* 7.

ZHENG, Z., LAURITZEN, J. S., PERLMAN, E., ROBINSON, C. G., NICHOLS, M., MILKIE, D., TORRENS, O., PRICE, J., FISHER, C. B., SHARIFI, N., CALLE-SCHULER, S. A., KMECOVA, L., ALI, I. J., KARSH, B., TRAUTMAN, E. T., BOGOVIC, J. A., HANSLOVSKY, P., JEFFERIS, G. S. X. E., KAZHDAN, M., KHAIRY, K., SAALFELD, S., FETTER, R. D. & BOCK, D. D. 2018. A Complete Electron Microscopy Volume of the Brain of Adult Drosophila melanogaster. *Cell,* 174**,** 730-743.e22.

Fig 1

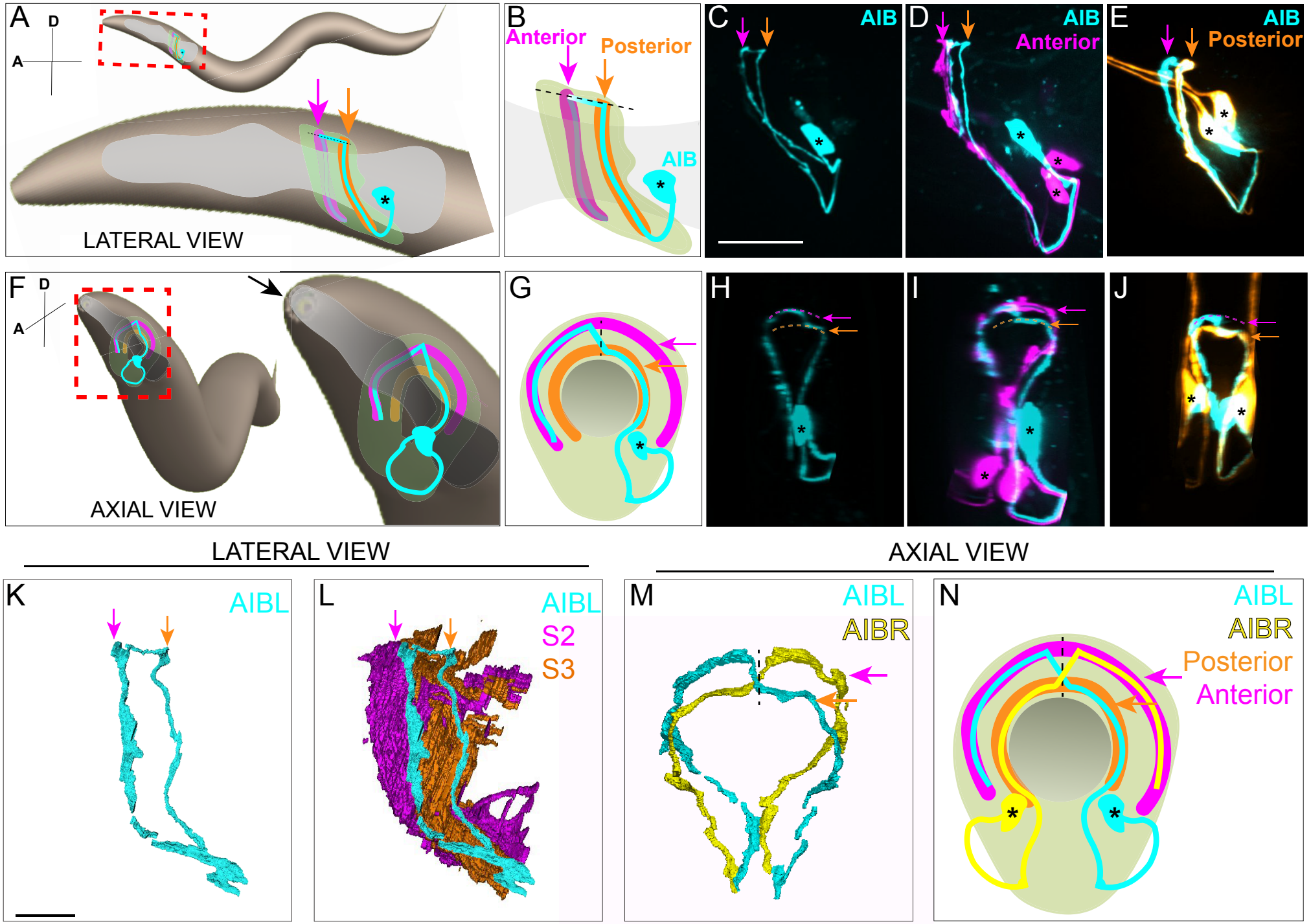
A
D
A
LATERAL VIEW
B
Anterior
Posterior
AIB
C
AIB
D
AIB
Anterior
E
AIB
Posterior
F
D
A
AXIAL VIEW
G
H
I
J
LATERAL VIEW
AXIAL VIEW
K
AIBL
L
AIBL
S2
S3
M
AIBL
AIBR
N
AIBL
AIBR
Posterior
Anterior

Fig 2

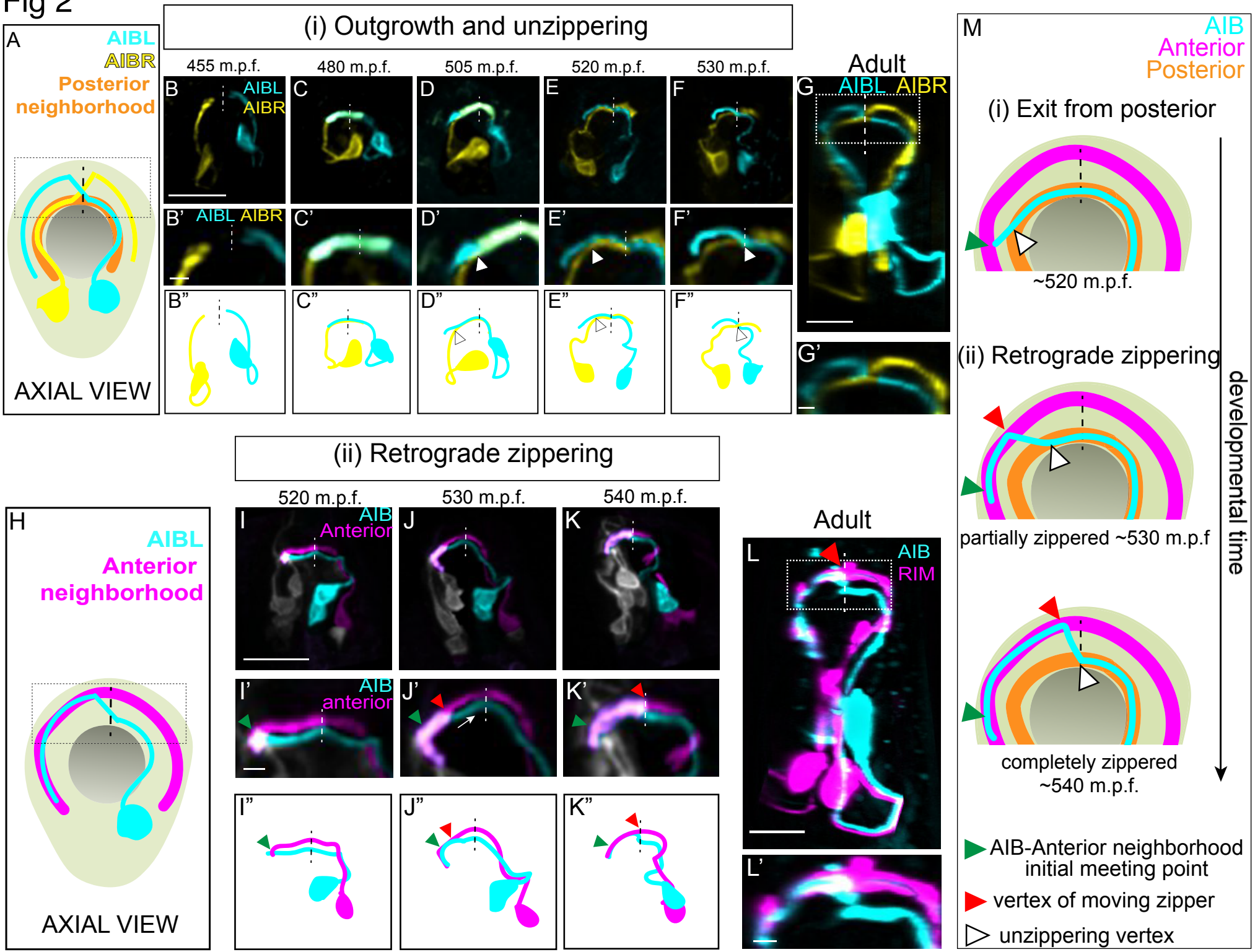
A
AIBL
AIBR
Posterior neighborhood
AXIAL VIEW
(i) Outgrowth and unzippering
455 m.p.f.
480 m.p.f.
505 m.p.f.
520 m.p.f.
530 m.p.f.
Adult
B
C
D
E
F
G
AIBL
AIBR
B'
C'
D'
E'
F'
B"
C"
D"
E"
F"
G'
(ii) Retrograde zippering
520 m.p.f.
530 m.p.f.
540 m.p.f.
H
AIBL
Anterior neighborhood
AXIAL VIEW
I
J
K
AIB
Anterior
I'
J'
K'
AIB
anterior
I"
J"
K"
Adult
L
AIB
RIM
L'
M
AIB
Anterior
Posterior
(i) Exit from posterior
~520 m.p.f.
(ii) Retrograde zippering
partially zippered ~530 m.p.f
completely zippered
~540 m.p.f.
developmental time
AIB-Anterior neighborhood initial meeting point
vertex of moving zipper
unzippering vertex

Fig 3

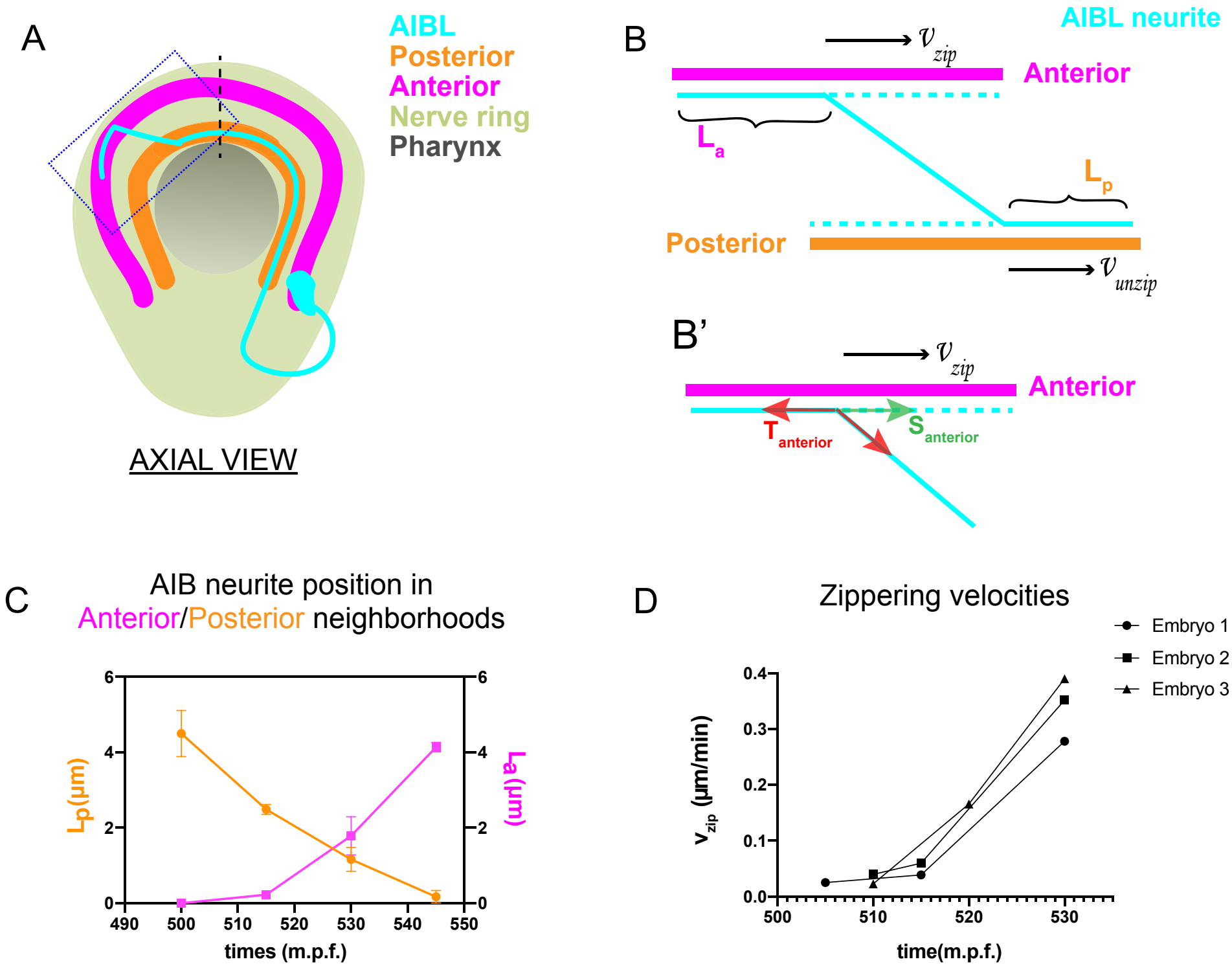
A
AIBL
Posterior
Anterior
Nerve ring
Pharynx
AXIAL VIEW
B
AIBL neurite
v_{zip}
Anterior
L_a
L_p
Posterior
v_{unzip}
B'
v_{zip}
Anterior
$T_{anterior}$
$S_{anterior}$
C
AIB neurite position in
Anterior/Posterior neighborhoods
L_p(µm)
L_a(µm)
times (m.p.f.)
D
Zippering velocities
Embryo 1
Embryo 2
Embryo 3
v_{zip} (µm/min)
time(m.p.f.)

Fig 4

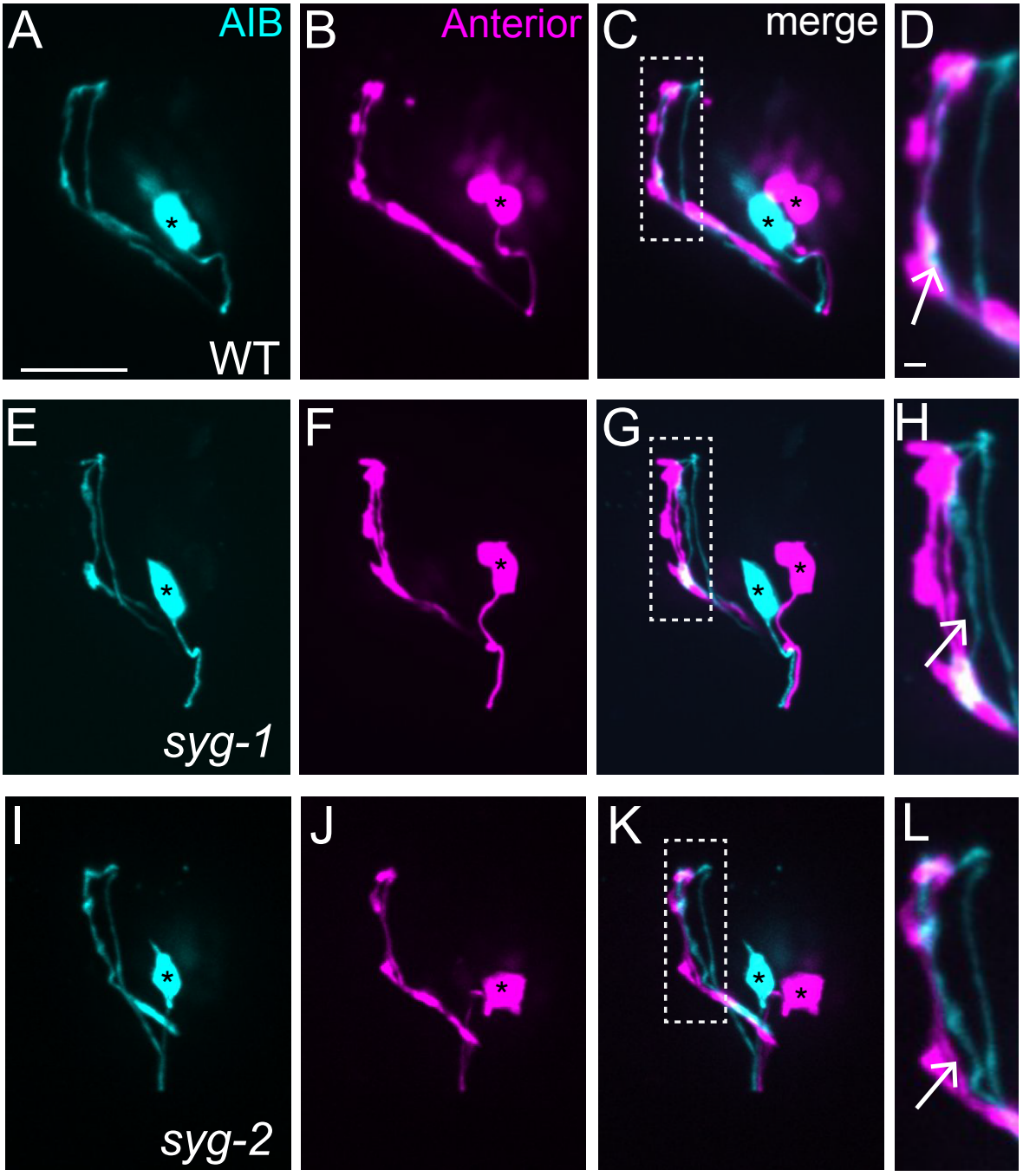
A
AIB
WT
B
Anterior
C
merge
D
E
syg-1
F
G
H
I
syg-2
J
K
L

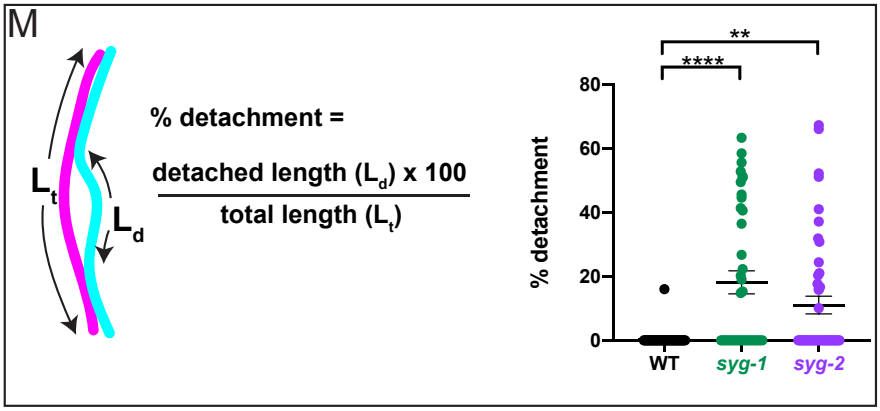
M
L_t
L_d
% detachment =
detached length (L_d) x 100
total length (L_t)
% detachment
80
60
40
20
0
****
**
WT
syg-1
syg-2

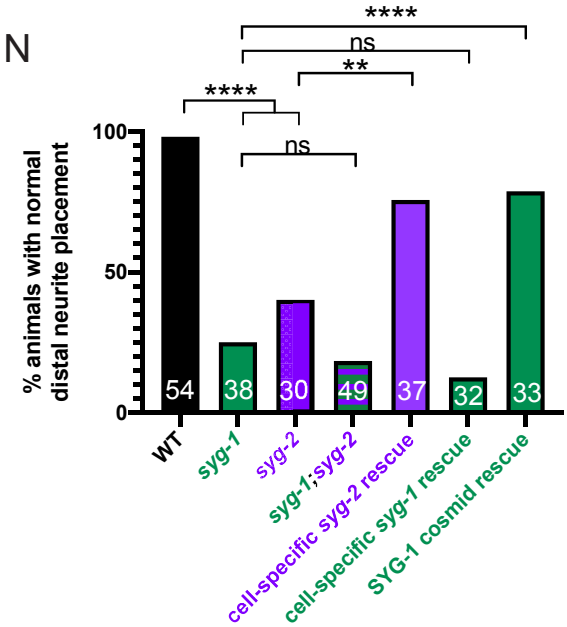
N
% animals with normal distal neurite placement
100
50
0
****
ns
**
****
ns
54
38
30
49
37
32
33
WT
syg-1
syg-2
syg-1;syg-2
cell-specific syg-2 rescue
cell-specific syg-1 rescue
SYG-1 cosmid rescue

Fig 5

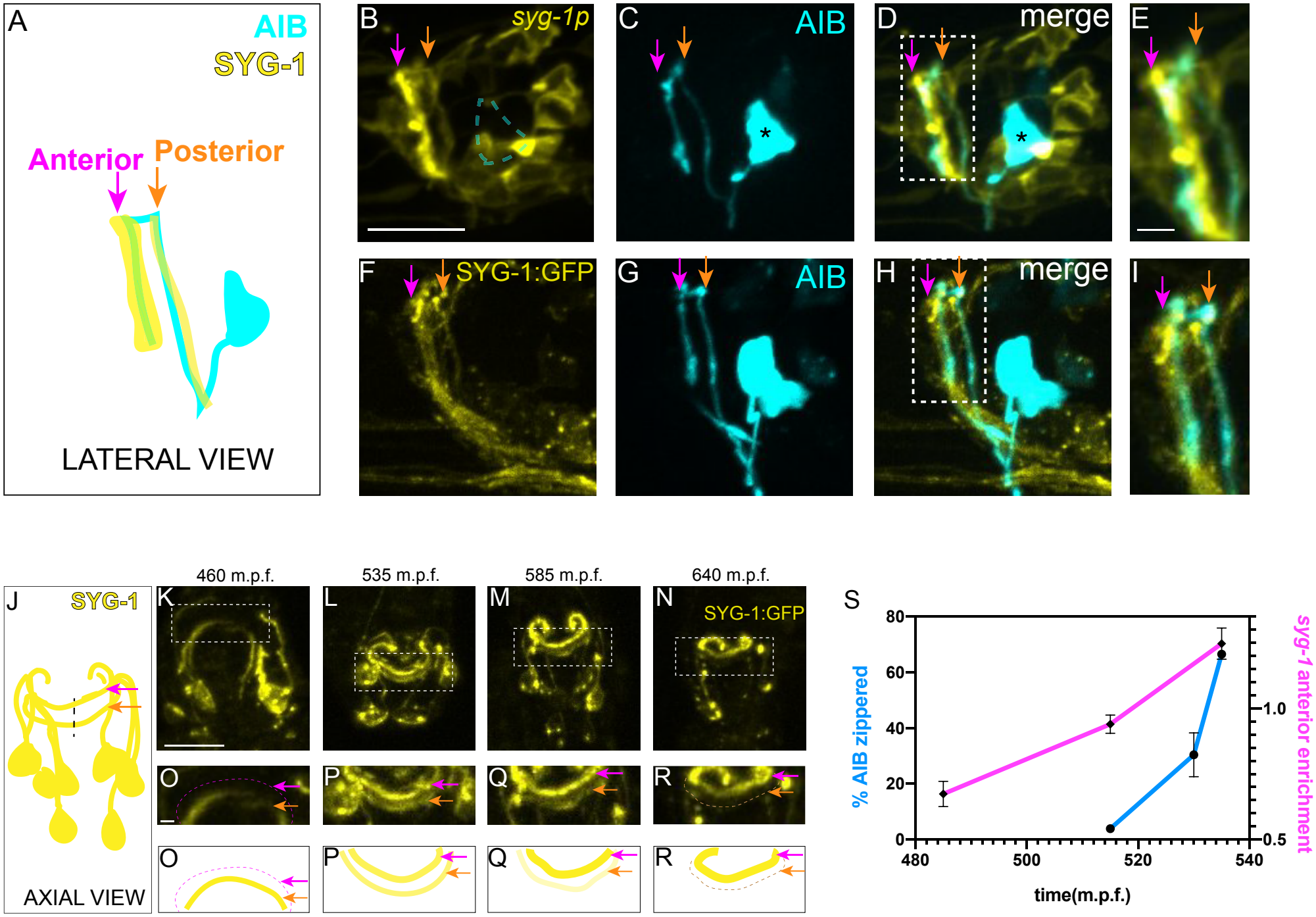
A
AIB
SYG-1
Anterior
Posterior
LATERAL VIEW
B
syg-1p
C
AIB
D
merge
E
F
SYG-1:GFP
G
AIB
H
merge
I
J
SYG-1
AXIAL VIEW
460 m.p.f.
535 m.p.f.
585 m.p.f.
640 m.p.f.
K
L
M
N
SYG-1:GFP
O
P
Q
R
S
% AIB zippered
syg-1 anterior enrichment
time(m.p.f.)
0
20
40
60
80
480
500
520
540
0.5
1.0

Fig 6

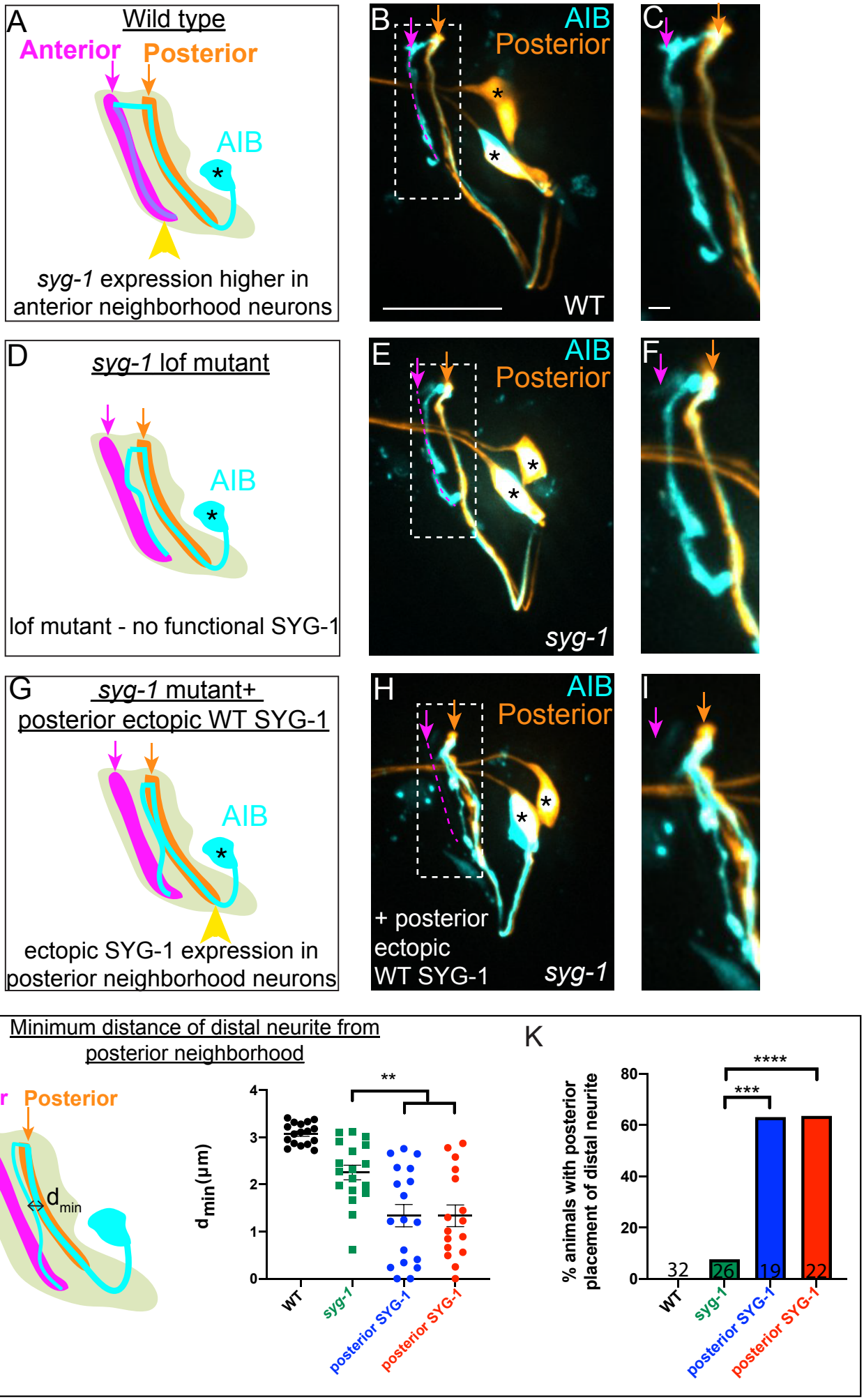
A
Wild type
Anterior
Posterior
AIB
syg-1 expression higher in anterior neighborhood neurons
B
AIB
Posterior
WT
C
D
syg-1 lof mutant
AIB
lof mutant - no functional SYG-1
E
AIB
Posterior
syg-1
F
G
syg-1 mutant+ posterior ectopic WT SYG-1
AIB
ectopic SYG-1 expression in posterior neighborhood neurons
H
AIB
Posterior
+ posterior ectopic WT SYG-1
syg-1
I
J
Minimum distance of distal neurite from posterior neighborhood
Anterior
Posterior
d min
d min (µm)
**
WT
syg-1
posterior SYG-1
posterior SYG-1
K
% animals with posterior placement of distal neurite
****
***
32
26
19
22
WT
syg-1
posterior SYG-1
posterior SYG-1

Fig 7

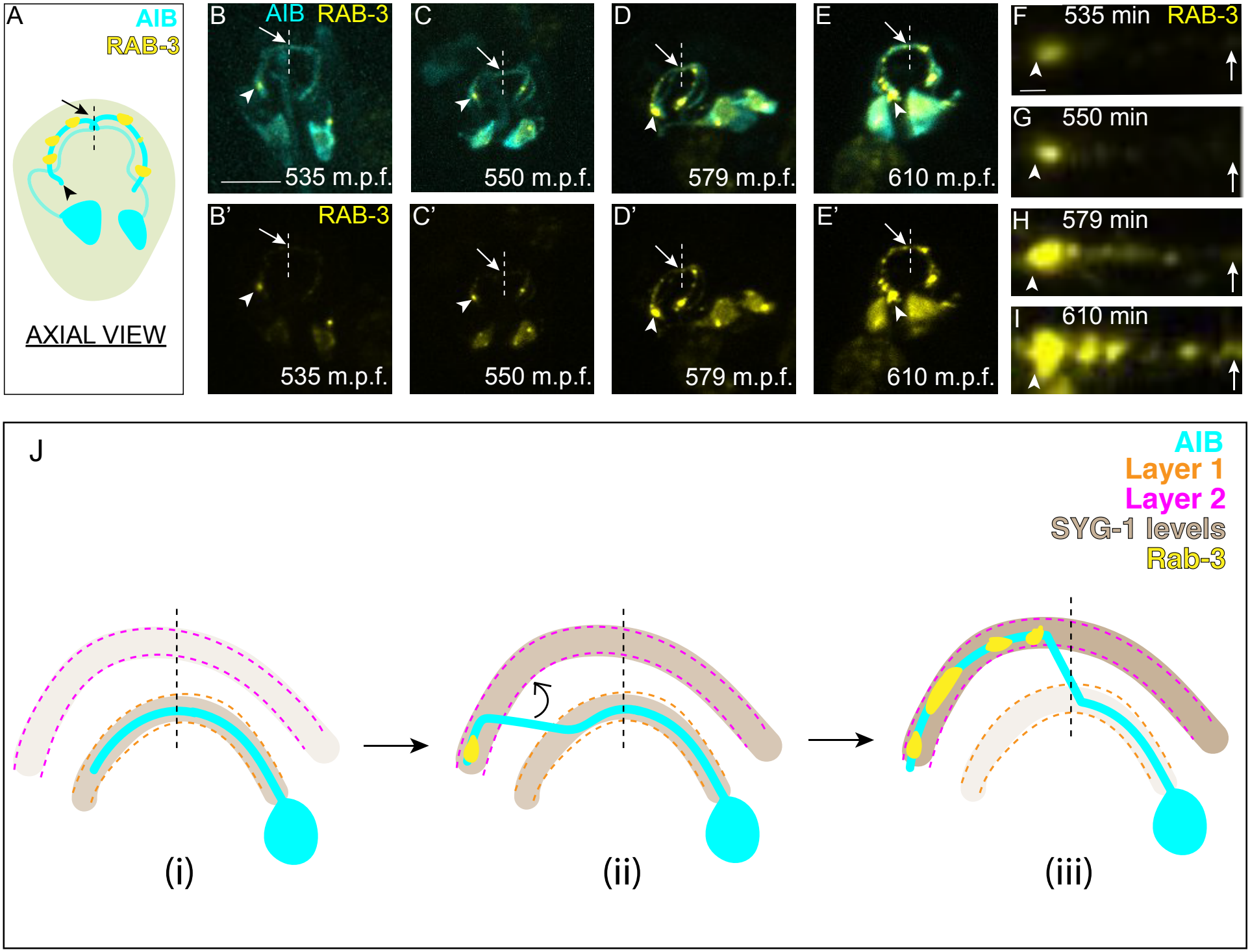
A
AIB
RAB-3
AXIAL VIEW
B
AIB
RAB-3
535 m.p.f.
C
550 m.p.f.
D
579 m.p.f.
E
610 m.p.f.
F
535 min
RAB-3
G
550 min
H
579 min
I
610 min
B'
RAB-3
535 m.p.f.
C'
550 m.p.f.
D'
579 m.p.f.
E'
610 m.p.f.
J
AIB
Layer 1
Layer 2
SYG-1 levels
Rab-3
(i)
(ii)
(iii)